

# **Abstract**

blid bla asdfjwaejhafiauwefawghaweüojawrgjaw



# **Kurzfassung**



# Contents

<b>1</b>	<b>Introduction</b>	<b>1</b>
<b>2</b>	<b>Theory</b>	<b>3</b>
2.1	Interaction of X-rays with matter . . . . .	3
2.1.1	Complex refraction-index . . . . .	3
2.1.2	Attenuation . . . . .	4
2.1.3	Refraction . . . . .	5
2.2	Phase contrast imaging . . . . .	5
2.2.1	Wave-Front propagation . . . . .	6
2.2.2	Talbot effect . . . . .	6
2.2.3	Grating interferometer . . . . .	8
2.2.4	Grating Types . . . . .	8
2.2.5	Coherence requirements . . . . .	9
2.2.6	Visibility and Phase stepping routine . . . . .	11
2.2.7	Magnification in curved wave geometry . . . . .	15
2.2.8	Induced uncertainty by an expanded edge thickness at different magnifications . . . . .	17
2.3	Spatial system response . . . . .	20
2.3.1	Real- and frequency-space response functions . . . . .	21
2.3.2	Edge- and Line- spread function (ESF/LSF) . . . . .	22
2.3.3	PSF of a complex system . . . . .	23
<b>3</b>	<b>The Setup</b>	<b>25</b>
3.1	The source . . . . .	26
3.1.1	Dimensions and structure . . . . .	26
3.1.2	properties . . . . .	27
3.2	Sample handling . . . . .	28
3.3	detector properties . . . . .	29
<b>4</b>	<b>Time- Power-Stability</b>	<b>31</b>
4.1	Time-stability . . . . .	31
4.2	Power-stability . . . . .	33
<b>5</b>	<b>SSR characterization</b>	<b>37</b>
5.1	Knife edge measurements . . . . .	37

5.1.1	Data acquisition . . . . .	37
5.1.2	Data processing . . . . .	40
5.1.3	Results . . . . .	43
5.2	Measurements using a Resolution-target . . . . .	44
5.2.1	Data acquisition . . . . .	44
5.2.2	Data processing . . . . .	44
<b>6</b>	<b>Spectra measurements</b>	<b>45</b>
<b>7</b>	<b>Comparison of different grating interferometer constellations</b>	<b>47</b>
<b>8</b>	<b>summary and outlook</b>	<b>49</b>
	<b>List of Figures</b>	<b>50</b>
	<b>List of Tables</b>	<b>51</b>
	<b>Acronyms</b>	<b>53</b>
	<b>Bibliography</b>	<b>55</b>

# **1 Introduction**



## 2 Theory

The focus of this thesis lies on the experimental characterization of the micro-focus X-ray setup at the biophysical chair E17. Special care is taken thereby on the source properties and the interferometric parts. Hence the underlying theory of the physical principles of this work are presented restricted on the most essential basics.

The interested reader is referred to the recommendations at the beginning of each section for a further detailed overview of the respective topic.

### 2.1 Interaction of X-rays with matter

X-rays are a part of the electromagnetic spectrum in between extreme ultraviolet and gamma radiation. The corresponding photon energies range from approximately 100 eV up to a few hundred keV. Since the discovery of X-rays by Wilhelm Conrad Roentgen in 1895, several different ways generating X-rays were developed and have been since then continuously improved. X-rays used for clinical applications are generally produced using conventional X-ray tubes. In an X-ray tube, electrons are produced by thermal emission from a heated cathode. Applying a strong electric field between cathode and anode the electrons are accelerated towards the anode. Upon hitting the anode the electrons are decelerated and emit a broad spectrum of X-rays, known as *Bremsstrahlung*. Additionally, radiation of characteristic energies depending on the anode material is emitted. Detailed description about X-ray sources and the interaction of X-rays with matter can be found in [1, 25]. The dependency between the energy and the resulting wavelength is given by:

$$\lambda [\text{\AA}] = \frac{hc}{E} = \frac{12.398}{E [\text{keV}]} \quad (2.1)$$

The wavelength of X-rays ranges e.g. from  $12.4 \times 10^{-10}\text{m}$  for 100 eV down to  $0.775 \times 10^{-11}\text{m}$  for 160 keV, whereby there is no upper limiting energy. The region of a few 100 eV is called soft X-rays, photons of higher energies are called hard X-rays.

#### 2.1.1 Complex refraction-index

Just like visible light, X-rays are electromagnetic waves, thus their behaviour when passing through matter can be described by the complex index of refraction  $n$ :[1]

$$n = 1 - \delta + i\beta. \quad (2.2)$$

$\delta$  and  $\beta$  depend on the material properties of the passed medium and the energy of the X-rays. A plane monochromatic wave without polarization propagating along the z-axis

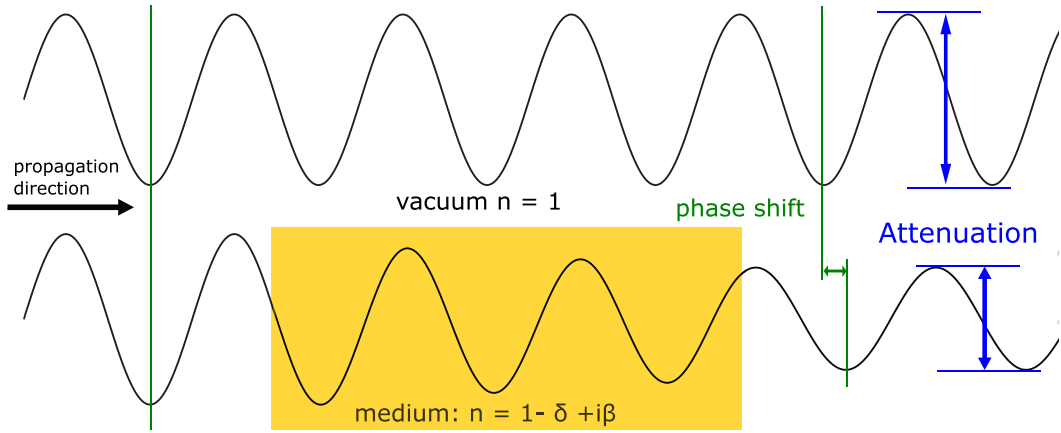


**Figure 2.1:** Drawing of two electromagnetic waves. The upper one propagates in vacuum, the lower wave propagates through a medium described by a complex index of refraction. This wave has an attenuated amplitude and a shifted phase compared to the wave propagation in vacuum. The attenuation and phase shift are depicted as blue and green arrows, respectively.

in vacuum ( $n = 1$ ), can be described by a scalar wave function  $\Psi(z)$ :

$$\Psi(z) = E_0 e^{ikz}. \quad (2.3)$$

Here  $E_0$  is the amplitude of the electric field and  $k = 2\pi/\lambda$  the wavenumber. Within a medium this equation changes to:

$$\Psi(z) = E_0 e^{inkz} = E_0 e^{(1-\delta+i\beta)ikz} = E_0 e^{(1-\delta)ikz} e^{-\beta kz}. \quad (2.4)$$

Here,  $\delta kz$  and  $e^{-\beta kz}$  describe the accumulated phase shift and the exponential loss of the waves amplitude after travelling a distance  $z$  through a medium, respectively. The waves and the respective losses are shown in Fig. 2.1. The macroscopic effects of these two are discussed separately in the following.

### 2.1.2 Attenuation

The attenuation of an electromagnetic wave corresponds to a loss of intensity of the beam. This macroscopic attenuation is over a broad energy range, dominated by two main effects: *photoelectric absorption* and *Compton scattering*, an incoherent and inelastic scattering process [1]. According to the *Lambert-Beer Law*, the relation between the reduction of intensity and the imaginary part of the refraction index,  $\beta$ , of an object is given by:

$$I(d) = I_0 e^{-2\beta kd} = I_0 e^{-\mu d}, \quad (2.5)$$

with the linear attenuation coefficient  $\mu = 4\pi\beta/\lambda$  and  $I_0$  the initial intensity of the wave passing through the object [6]. The linear absorption coefficient  $\mu$  depends on the

incoming wavelength, and thus on the corresponding X-ray energy and the composition of the illuminated material. The formation of images in attenuation based X-ray imaging is a measure of the material dependent attenuation coefficients and the corresponding intensity loss of the X-ray beam after propagating through the studied object.

### 2.1.3 Refraction

For a medium of thickness  $d$ , the total phase shift  $\Phi$  is given by the real part of the refractive index,  $\delta k z$ , in equation 2.4:

$$\Phi = \delta k d. \quad (2.6)$$

For an object which has a change in thickness or the refractive index in the direction normal to the wave propagation, the total phase shift depends on the position of the sample. The consequence of this is a change of the propagation direction of the incoming X-ray beam. In general, this angle of refraction  $\alpha$  is equivalent to the local gradient of the phase shift perpendicular to the direction of incidence - in this case the  $z$ -direction-divided by the wave vector  $k = 2\pi/\lambda$ . For reasons of simplicity the problem here is restricted to the  $x$ -direction and thus the gradient eases to a simple derivative in  $x$ . The corresponding equation for the refraction angle then simplifies to:

$$\alpha = \frac{1}{k} \frac{\partial \Phi(x)}{\partial x}. \quad (2.7)$$

One main difference between visible light and X-rays, is the deviation of the refractive index from unity. On the one hand for visible light the refractive index can deviate over a wide range from 1, on the other hand for X-rays the deviation is very narrow. Considering the dependencies of refractive index decrement  $\delta$  this behaviour becomes easily clear. The material dependent term  $\delta$  also strongly depends on the energy of the X-ray beam, and is described as:

$$\delta = \frac{\lambda^2 r_e n_e}{2\pi}, \quad (2.8)$$

with the classical electron radius  $r_e = 2.818 \times 10^{-15}$ m and the electron density  $n_e$  of the material. As example for energies above 12.4 keV  $\equiv \times 10^{-10}$ m  $\delta$  is of the order of  $10^{-6}$ . This very small effect leads to very small refraction angles, which makes detecting X-ray refraction very difficult. On the elementary particle level, the process of X-ray refraction can be described by the elastic scattering, also known as *Thomson scattering* [1], of the photons at the electrons of the material the wave is passing through. The key to phase contrast imaging declines to the measurement of these refraction angles. One way how this can be done is explained further in the following section.

## 2.2 Phase contrast imaging

There are several different approaches on making tiny changes of an X-ray beams direction visible, but the focus lies here on the grating-based phase contrast imaging technique. For further detail about the other techniques and the topics in this section see: [4, 5, 16, 19, 25, 28, 29].

### 2.2.1 Wave-Front propagation

One way to describe electromagnetic waves is to consider them as a wave front. According to *Huygens principle* a wave-front can be described at any time by the sum of spherical wavelets distributed over the whole wave-front. This leads to the Fresnel diffraction integral (valid in the homonym *Fresnel regime* also near-field regime) , which is the integral over the contribution of all spherical waves:

$$\Psi(x, y, z) = \frac{e^{ikz}}{i\lambda z} \int \int \Psi(x_0, y_0, 0) e^{\frac{ik}{2z}((x-x_0)^2 + (y-y_0)^2)} dx_0 dy_0, \quad (2.9)$$

whereby  $x_0$  and  $y_0$  are the values in the  $z = 0$  plane. With this equation it is possible to calculate the wave-front at any time. The propagation itself can be considered as the convolution of the wave function  $\Psi(x, y, z)$  at  $z = z_0$  and a so called propagator function  $h_d$ :

$$h_d = \frac{e^{ikd}}{i\lambda d} e^{\frac{ik(x^2+y^2)}{2d}}, \quad (2.10)$$

where  $d$  denotes the propagation distance. With the convolution theorem, stating that the Fourier transform of a convolution of two functions is equal to the product of the Fourier transforms of these two functions, it is possible to propagate the wave-front over a distinct distance by simple multiplication in Fourier space. Thereby the Fourier space propagator function  $\tilde{P}_d(k_x, k_y)$  is the Fourier transform of the propagator function in real space, denoted by:

$$\tilde{P}_d(k_x, k_y) = \mathcal{F}(h_d(x, y)) = e^{ikd} e^{\frac{-id(k_x^2+k_y^2)}{2k}}, \quad (2.11)$$

which can be shown with simple physical considerations [4].

### 2.2.2 Talbot effect

The Fourier space propagator is an easy and efficient way to calculate the wave-front at any given propagation distance. In the case of a spatially periodic wave-front, such as a sine or a cosine modulated wave-front, a self-image after a distinct propagation distance can be assumed. That a periodic wave-front repeats itself after a distinct propagation distance was first discovered by Henry Fox Talbot in 1836. This distance is known as the Talbot distance  $d_T$  [24]. In his studies he used visible light and a grating to create a periodic wave-front, but the effect is also valid for the X-ray range [8].

The distinct distance where the wave-front recreates can be simply calculated by multiplication of equation 2.3 with the propagator function defined in equation 2.2.1. With this calculation it can be shown that a periodic wave-front repeats itself at a certain distance  $d_T$ :

$$d_{T_n} = \frac{2np^2}{\lambda}, \quad (2.12)$$

whereby  $n = 1, 2, 3, \dots$  indicates the Talbot-order. Considering a well known wave-function, for example a step-function induced by a periodic grating, so called *Fractional*

*Talbot distances* arise [4]. A general relation for the fractional distances, created by a phase grating with a phase shift of  $\pi/2$  is given by:

$$d_{T_{frac}} = \frac{np^2}{8\lambda}, \quad (2.13)$$

where n again denotes the Talbot order and p the period of the grating. A feature occurs at half the Talbot distance where the initial intensity pattern repeats exactly, besides of a shift in direction perpendicular to the grating lines. However, at certain fractional Talbot distances, patterns of alternating low and high intensity arise, which is of great interest for phase contrast imaging using gratings. A main problem is the spectrum illuminating the grating, because the exact revival of the wave-front only appear, if monochromatic waves are used. Otherwise the pattern lute, due to the fact of to less coherence. Thus the Talbot carpet has only bright and dark regions, which can be seen on the right side of figure 2.2. But nevertheless, phase contrast imaging is still possible at fractional Talbot distances, also in this case.

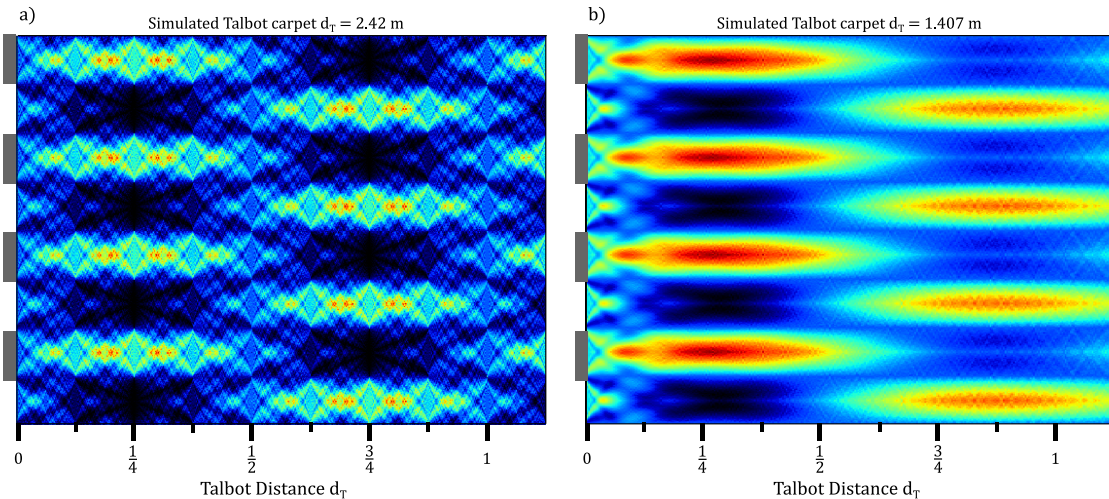


**Figure 2.2:** Simulated Talbot-carpets for a gold grating with a duty cycle of 0.5 a phase shift of  $\pi/2$  and a grating period of  $5\text{ }\mu\text{m}$ . a) Intensity distribution for a monochromatric X-ray source with an x-ray energy of 60 keV. Besides a phase shift the initial wave-front revives at half and after one Talbot distance  $d_T$ . In between a strong periodic intensity modulation at  $1/4$  and  $3/4$   $d_T$  occurs, which matches the period of the simulated grating. b) Simulation results for a polychromatric source, described by a tungsten spectrum with 60 kVp. Due to the polychromatric spectrum the resulting pattern is a superposition of the individual patterns of all energies. The Talbot distance depends on the wavelength and therefore the intensity modulations are smeared out. Hence just high and low contrast regions are still observable.

### 2.2.3 Grating interferometer

As mentioned in the sections above the underlying principle of phase contrast imaging is to quantify the refractive index distribution of a sample, or in other words to measure the induced angle of refraction onto the transmitted X-ray wave. The idea behind using a grating interferometer for this method is that a small angular change of the wave-front leads to a transverse shift of the interference pattern induced by the grating. In the optimum case of a perfect wave-front, just two gratings are needed making this technique applicable. In practice, a third grating, is often used to perform grating interferometry measurements at conventional X-ray sources. Such a setup known as Talbot-Lau interferometer is shown in Fig:2.3. Hereby the usual first grating, denoted by  $G_1$ , induces a periodic phase-shift onto the wave-front and the second grating,  $G_2$ , serves as analyser grating. The last grating,  $G_2$ , is ideally placed at a fractional Talbot distance and makes detection of the very fine interference pattern with standard X-ray detectors feasible. Regions around odd fractional Talbot distances have a high visibility of the interference pattern, which is explained in further detail in 2.2.6 and can also be seen in figure 2.2 on the left side, e.g. speaking of  $d = 1/4 d_T$ , where the Talbot-carpet has a region of highest contrast. In general there is a huge lack between the optimum requirements and the existing properties of source and gratings. Nevertheless the requirements of the source can be overcome by introducing a third grating,  $G_0$ , right behind the source. At this installation the third grating  $G_0$ , which is an absorption grating, works as a mask for the spacious source, normally used at clinical applications or at laboratories, with a source size unable to provide sufficient spatial coherence. This grating slices the source in evenly spaced individually coherent line-sources which interfere with each-other. In such a setting, it is important that the following condition is fulfilled:

$$p_0 = p_2 \times \frac{l}{d}. \quad (2.14)$$

Only then individual line-sources interfere constructively and can contribute to the imaging process. Hereby are  $p_0$  and  $p_2$  the respective grating period,  $l$  is the distance between  $G_0$  and  $G_1$  and  $d$  the distance between  $G_1$  and  $G_2$ . Using this alignment the total source size  $S$  is only responsible for the final resolution of the image given by  $Sd/l$  and spatial resolution is decoupled from spatial coherence, which allows the use of X-rays with very small coherence length in both directions [19].

### 2.2.4 Grating Types

In general there are two different grating types, absorption and phase gratings. As one can imagine, the main property of absorption gratings is their high ability to strongly absorb X-rays. For that reason, the material they are made of has to have high electron density, and thus a high atomic number  $Z$  e.g. lead or gold. The better choice for the production is gold, at one hand, because the absorption performance compared to lead is twice as good. At the other hand the electroplating mechanisms are better understood. Overcoming the softness of gold, absorption gratings are formed using a support layer generally made of silicon, because the handling of Si wavers and their

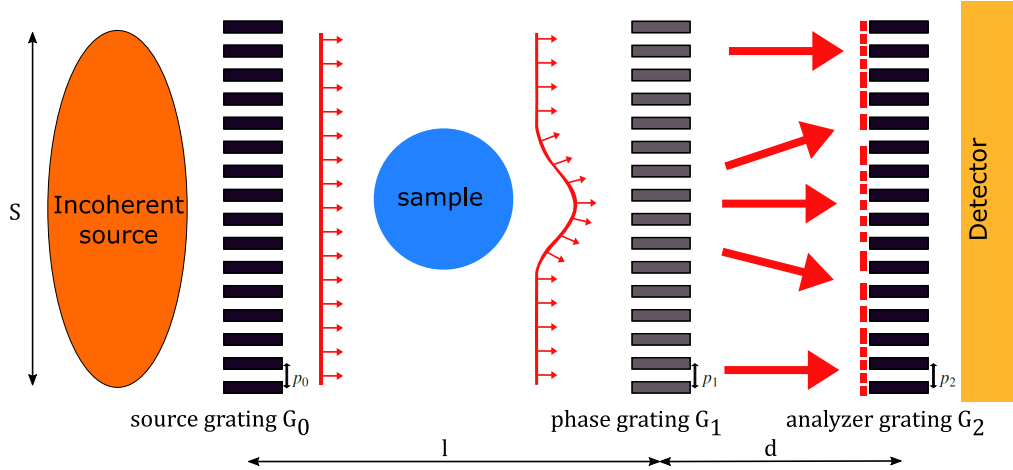


**Figure 2.3:** Sketch of a Talbot-Lau interferometer. Underlying principle: The source grating  $G_0$  induces individual coherent, but not mutual coherent, line-sources. Refraction caused by intrinsic sample properties, induces distortions of the wave-front. These very tiny changes of the interference pattern created by the phase grating  $G_1$ , are then recorded by a standard X-ray detector, by dint of  $G_2$ .

subsequent treatment is well known. There are several ways to produce an absorption grating, one is the Lithography and Galvanization (LIGA) process [? ]. During this process, a supporting structure is produced from a photo-resist using x-ray lithography and deep reactive ion etching. The trenches are then filled with gold by electroplating. **markus fragen** In the main part of figure 2.4 such an absorption grating with a gold height of  $50\ \mu\text{m}$  and a grating period of  $2.4\ \mu\text{m}$  is shown. In general, a higher gold filling is preferred as it corresponds to a better X-ray absorption. However, forming such high gratings with a period of only a few micrometers is very difficult. Nowadays, grating heights up to  $200\ \mu\text{m}$  are possible over large areas [? ]. Phase gratings usually consist of low Z materials in order to avoid absorption when introducing the desired phase-shift. Due to the fact that high absorption is not desired, the height of phase gratings furthermore is way lower than that of absorption gratings. The inset of figure 2.4 shows such a phase grating made of silicon with a height of  $22\ \mu\text{m}$  and a period of  $4\ \mu\text{m}$ , but there are also various combinations of materials forming such gratings e.g. a silicon grating electroplated with nickel, which is usually used at the setup, used during the work presented in this thesis. For Further reading about production mechanisms and the different grating types see: [? ]

## 2.2.5 Coherence requirements

As mentioned in section 2.2.3 the coherence requirements of the source can be relaxed by inserting a third grating ( $G_0$ ) right behind the source. In this section an overview

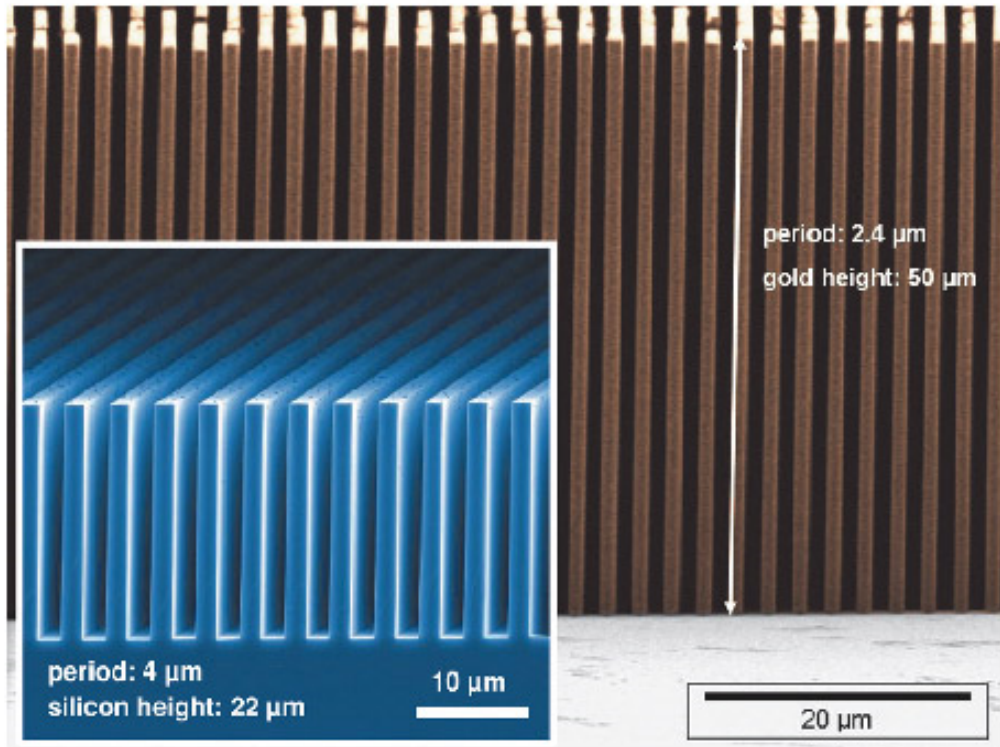


**Figure 2.4:** Different types of deep micro-structured gratings feasible for X-ray grating interferometry. Dependent on the properties of the respective grating phase and/or amplitude modulation is possible. In the main picture a Gold absorption grating is depicted manufactured at KIT. At the inset a pure Silicon phase grating made at the PSI is shown. (source: <http://www.esrf.eu/UsersAndScience/Publications/Highlights/2010/imaging/img02>)

about the relevant equations and parameters are introduced, in order to get a feeling about the required dimensions. For further reading see [16, 28]. There are two important parameters in order to describe the coherence properties of X-rays. On one hand, the longitudinal coherence length is related to the bandwidth of the used source spectrum. Concerning the longitudinal coherence an approximate expression for the required monochromaticity yielding to good fringe contrast in the interference pattern is[29]

$$\frac{\lambda_0}{\Delta\lambda} \gtrsim n. \quad (2.15)$$

Here  $\lambda_0$  denotes the design wavelength of the setup,  $\Delta\lambda$  the width of the luting of the design wavelength and  $n$  the order of the Talbot distance from equation 2.12. This expression implies the possibility, to apply a polychromatic source for grating interferometry, without loosing significant contrast quality between the particular fringes. For

that reason, this section focusses on the spatial coherence requirements, because their influence onto the resulting signal is much higher. As mentioned in section 2.2.3 for the case of just considering plane-waves the final resolution of an image is given by  $Sd/l$ . A sketch of these variables is shown in Fig: 2.3 where  $S$  is the finite source size,  $l$  the distance between  $G_0$  and  $G_1$  and  $d$  the distance between  $G_1$  and  $G_2$ , respectively. There are several common definitions for the transversal coherence length  $\zeta_s$  existing alongside to each other so here  $\zeta_s$  is defined as [29]:

$$\zeta_s = \frac{\lambda l}{S}, \quad (2.16)$$

where  $\lambda$  is the wavelength corresponding to the design energy of the interferometer. Typical values for an extended source size are about an square millimetre and an integrating distance of about one metre are  $\zeta_s \approx 10^{-8}$  m and for more advanced micro-focus tubes with much less power or synchrotrons  $\zeta_s \approx 10^{-6}$  m [19]. A comparison between typical and micro-focus X-ray tubes is given in chapter 3. In the following section a compendium of the phase-retrieval mechanism is shown with respect to the coherence requirements mentioned in this section.

## 2.2.6 Visibility and Phase stepping routine

**Visibility** The phase grating modulates the phase of the incoming wave-front, so that fringe pattern arise at the position of the analyser grating, which is placed at a fractional Talbot distance. Just concerning first order diffraction [28] this pattern has nearly a sinusoidal shaped intensity profile. The distance  $d$  is adjusted to the fractional Talbot-distances with the highest contrast (see Figure 2.2), where the minima of the intensity pattern drop down to zero<sup>1</sup>. Using completely coherent radiation, the intensity profile can be expressed by [28]:

$$I(x) = I_0(1 + \sin(\frac{2\pi x}{p_2})), \quad (2.17)$$

thereby  $x$  denotes the coordinate transversal to the grating lines,  $I_0$  the intensity before  $G_1$  and  $p_2$  the period of the fringes. The interferometer should be also designed in that way, that this period coincides with the analyser grating period. For an expanded source with size  $S$  with only partial coherent radiation, the observed intensity pattern changes to a convolution of a point-source with the projected source profile, with width  $w$ . If a Gaussian- shaped source is assumed for simplicity, the convolution results again in a Gaussian with the width

$$w = S \times \frac{d}{l}, \quad (2.18)$$

hereby  $S$  and  $w$  correspond to the full width at half maximum (FWHM) of the initial and the projected source profile, respectively. For the idealized case of a point-source the visibility  $V$ , which is equivalent to the *Michelson contrast* [? ], is unity, but for real

---

<sup>1</sup>This case is just valid assuming a perfect setup, with an infinitesimal source size, monochromatic radiation, perfect gratings with no defects and a perfect detector.

sources speaking of expanded ones like e.g. in Figure 2.3 the visibility drops below unity. The visibility is defined as

$$V = \frac{I_{max} - I_{min}}{I_{max} + I_{min}}, \quad (2.19)$$

where  $I_{max}$  and  $I_{min}$  denote the maximum and minimum intensity values of the fringe pattern from equation 2.17. Introducing  $I_{max}$  and  $I_{min}$  equation 2.17 results in:

$$I(x) = \frac{I_{max} + I_{min}}{2} + \frac{I_{max} - I_{min}}{2} \sin\left(\frac{2\pi x}{p_2}\right). \quad (2.20)$$

An analytical investigation of the convolution of a Gaussian with a sine, yields to an equation for the decrease of the visibility, corresponding to the projected source size  $w$  [28]:

$$V = e^{-(1.887w/p_2)^2}, \quad (2.21)$$

whereas the decrease of  $V$  has a Gaussian shape. From this equation it is possible to directly derive an inequality for the projected source size, dependent on the minimum required visibility  $V_0$  and the periodicity  $p_2$  of both the analyser grating  $G_2$  and the intensity pattern, to:

$$w \leq 0.53p_2\sqrt{\ln(V_0)}. \quad (2.22)$$

As one can see in Figure 2.5 the resulting visibility is extremely dependent on the Talbot-distance  $d_T$ . As mentioned in section 2.2.2 the highest visibility, independent of dealing with monochromatic or polychromatic radiation, occurs always near the fractional Talbot-distances. For the monochromatic case it matches exact the fraction's, in the polychromatic case the maxima of the visibility are slightly shifted towards bigger distances, due to the superposition of the different Talbot-distances for each energy of the spectrum. Due to the dependence of the projected source size  $w$  on the distance between  $G_1$  and  $G_2$ , a fractional Talbot-distance with maximum visibility, e.g.  $d = p^2/2\lambda$ , can be substituted in the equation for the projected source size 2.18. With this the equation for  $w$  as a function of the Talbot-distance and -order derives to:

$$w = S \times \frac{np_2^2}{2\lambda l} = \frac{np_2^2}{2\zeta_s}, \quad (2.23)$$

where for the last step the coherence length  $\zeta_s$  is substituted. With this relation the equation for the visibility, 2.21, can be rewritten as a function of the spatial coherence length, resulting in [28]:

$$V = e^{-(0.94np_2/\zeta_s)^2}, \text{ and thus again } \Rightarrow \zeta_s \geq \frac{0.94np_2}{\sqrt{\ln(V_0)}}. \quad (2.24)$$

In order to get a feeling for the behaviour of this formulas for real experiments a few numerical examples are mentioned. As one can note on the left side of Fig. 2.2 the first order Talbot-distance occurs at 2,42 m, which is yet a big distance in a standard lab environment, because the dimensions of the installations have to fit into a quite small hutch due to space restrictions. For that reason higher Talbot orders  $n > 1$  can be

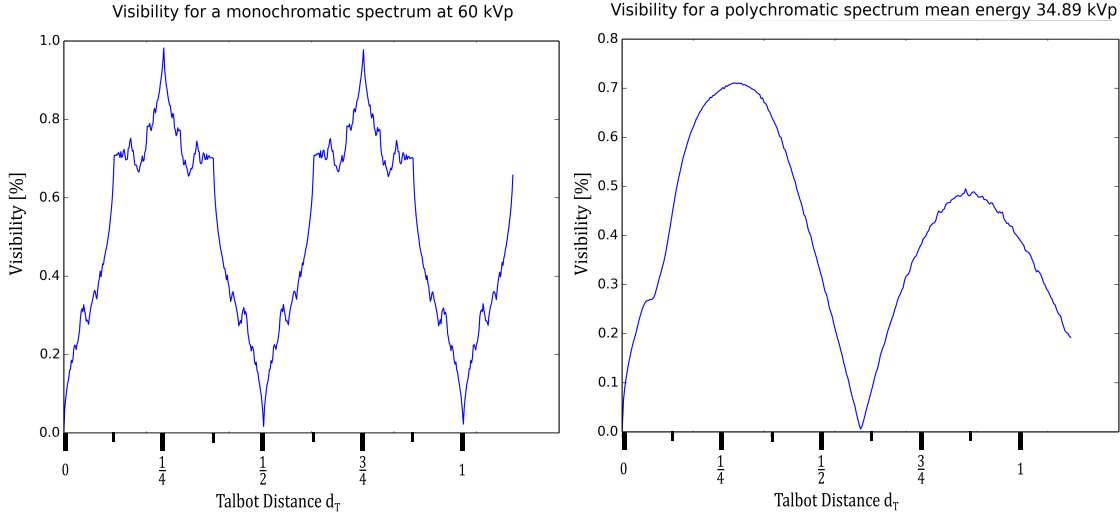


**Figure 2.5:** Simulated visibility as a function of the Talbot-distance  $d_T$ , corresponding to the shown Talbot-carpets in Fig. 2.2. On the left side the visibility for a monochromatic source is shown. In accordance to theory the maximum is reached at odd fractional Talbot-distances. On the right side the visibility is smeared out and no sharp peaks occur, due to the fact of the loss of the monochromaticity of the beam. Nevertheless is the loss of visibility within a small distance a bigger disadvantage for conventional X-ray sources.

usually neglected because of space restrictions. The grating-period of the analyser grating used in general at the setup ,mentioned at the beginning of this chapter, is  $10\text{ }\mu\text{m}$  and assuming a required minimum visibility of  $V_0 = 0.2$ , the required projected source size results in  $w \leq 6.7\text{ }\mu\text{m}$ , according to equation 2.22. Or in other words the transversal coherence length defined in equation 2.24 becomes  $\zeta_s \geq 7.41\text{ }\mu\text{m}$ . These values are for a low required visibility quite small, yet and mostly far out of range for conventional sources, but nevertheless as mentioned above is this technique applicable inducing a source grating.

**Phase stepping routine** In the next short paragraph the phase stepping-routine, where the defined relations above, especially equation 2.17 and 2.19 play an important rule is explained. The reader more interested in detail see: [4, 5, 12, 16, 18]. What is done in this procedure can be explained in a few simple words: "Move one of the three gratings perpendicular to the beam direction and vertical to the grating lines, while holding the other two at fixed position, and record how the intensity pattern varies over different grating positions for each individual pixel". Again just one direction is taken into account, because in general depending on the orientation of the grating lines phase information is just acquired, if the stepping moves along the axis perpendicular to the

grating lines.<sup>2</sup> Otherwise no information is recovered as one can imagine, because the pattern will not change due to the fact ,that there is no relative change between the distinct grating lines. For a more precise explanation Equation 2.17 is rewritten in a slightly different way, such that the intensity of every point  $x_d$  of the intensity pattern is expressed by

$$I(x_d, y = 0) = a_0 + a_1 \sin(\Phi_d + \varphi), \quad \text{with } \Phi_d = \frac{2\pi}{p_2} x_d, \quad (2.25)$$

with the offset  $a_0$ , the amplitude  $a_1$  and the corresponding transverse shift  $\varphi$  of the intensity pattern [4]. This equation contains the first two terms of a Fourier series and obviously solving this equation three different positions have to be measured, because for three unknown at least three different equations are needed. So the stepping has to exceed at least three steps getting feasible information and the stepping range should cover one full period of the analyser grating  $G_2$ . Usually an odd number of stepping points is used, because a even number of sampling-steps causes no additional benefit [4]. In order to get a good approximation of the shape of the stepping-curve, the sampling rate over one period is extended to 7 steps for in this work, but there is basically no upper limit. It is at least a trade-off between better results and measurement-time. At each of this steps an intensity image is taken, meaning that the interference pattern is sampled in each detector pixel during the particular steps. Afterwards the variation of the intensity in each pixel is then translated into a stepping-curve of the oscillating intensity describable with the equation above. To retrieve just the phase-shift if the X-rays induced by the sample, also a reference stepping without any sample at the same stepping positions is required. With these two curves at hand three different imaging signals can be extracted at once from each pixel of the dataset as illustrated in Figure 2.6 (a-c). Here the superscripts  $o$  and  $r$  denote the object and reference frame, respectively:

- As depicted in Figure 2.6 a), the transmission of the object, which in this thesis is referred to as AMP signal is:

$$a_0 = \frac{a_0^o}{a_0^r}. \quad (2.26)$$

This signal is equivalent to conventional X-ray attenuation imaging and relies also on the same physical principles.

- Figure 2.6 b), shows the relative transverse shift of the interference pattern due to the angular refraction of the X-ray beam passing through the object. With equation 2.7 for the refracted angle and a given distance  $d$  between  $G_1$  and  $G_2$  and the period  $p_2$  of the intensity distribution, the transverse shift is dependent on the differential phase shift of the wave-front as

$$\varphi = \frac{d\lambda}{p_2} \frac{\partial \Phi(x)}{\partial x}. \quad (2.27)$$

---

<sup>2</sup>As long as the gratings are perpendicular to the beam and the grating lines tend at the same direction, it does not matter in which direction, x- or y-direction or any other combination of them, the gratings are put into the beam.

And the transverse shift of the stepping curve is given by

$$\varphi = \varphi^o - \varphi^r \quad (2.28)$$

There is likewise an abbreviation for this imaging signal known as Differential Phase Contrast (DPC)

- Analogue to equation 2.19 the visibility of the stepping curve can be defined as  $V = a_1/a_0$ , thus the relative visibility of the interference pattern becomes [18]

$$V = \frac{V^o}{V^r}. \quad (2.29)$$

The visibility in the object frame is reduced by the effect of small-angle scattering of the X-rays caused by sub-micron structures in the object, shown in Figure 2.6 c). In the following the relative visibility signal is called X-ray Dark-field Imaging (DCI).

These three properties are referred to as AMP, DPC and DCI projections throughout the remainder of this work. According to standard radiographic imaging the outcome of the different signals is a line integral over the respective quantity along the beam direction across the object, which yields two-dimensional projection images.

### 2.2.7 Magnification in curved wave geometry

In this small section a transition from the assumption of perfect plane waves in the latter sections, to a more real case of curved wave-fronts is described. By assuming a point like source the difference between the distance of source to object and source to detector, further denoted by  $SO^3$  and  $SD$ , respectively, induces a magnification factor of

$$M = \frac{SD}{SO}. \quad (2.30)$$

The geometrical considerations for this relation are shown in Figure 2.7 for the case of a grating with a period  $p$ . The image of the grating on the detector is magnified by a factor  $M$ . This magnification factor obviously also has to be taken into account, when installing the grating interferometer. Staying at the treatment of the grating as an object, the interference fringes induced by  $G_1$  also undergo the magnification and so the period changes from  $p_1$  to  $Mg_1$  [4]. A way to avoid this, is producing periodic gratings which compensate this effect or one has to adjust the gratings for the exact position. Otherwise a mismatch of the exact distance between  $G_1$  and  $G_2$  results in Moire fringes at the detector declining the signal. For example a Moire fringe per 100 grating lines occurs for a magnification differing just one percent from 1, and with a grating period  $p_1 = 5 \mu\text{m}$  it ends up with 2 Moire fringes per millimetre. Nevertheless this factor also changes the Talbot distance, thus also the fractional Talbot-distances between the two

---

<sup>3</sup>This nomenclature is chosen to be as general as possible. For the following considerations the phase grating  $G_1$  is referred as object

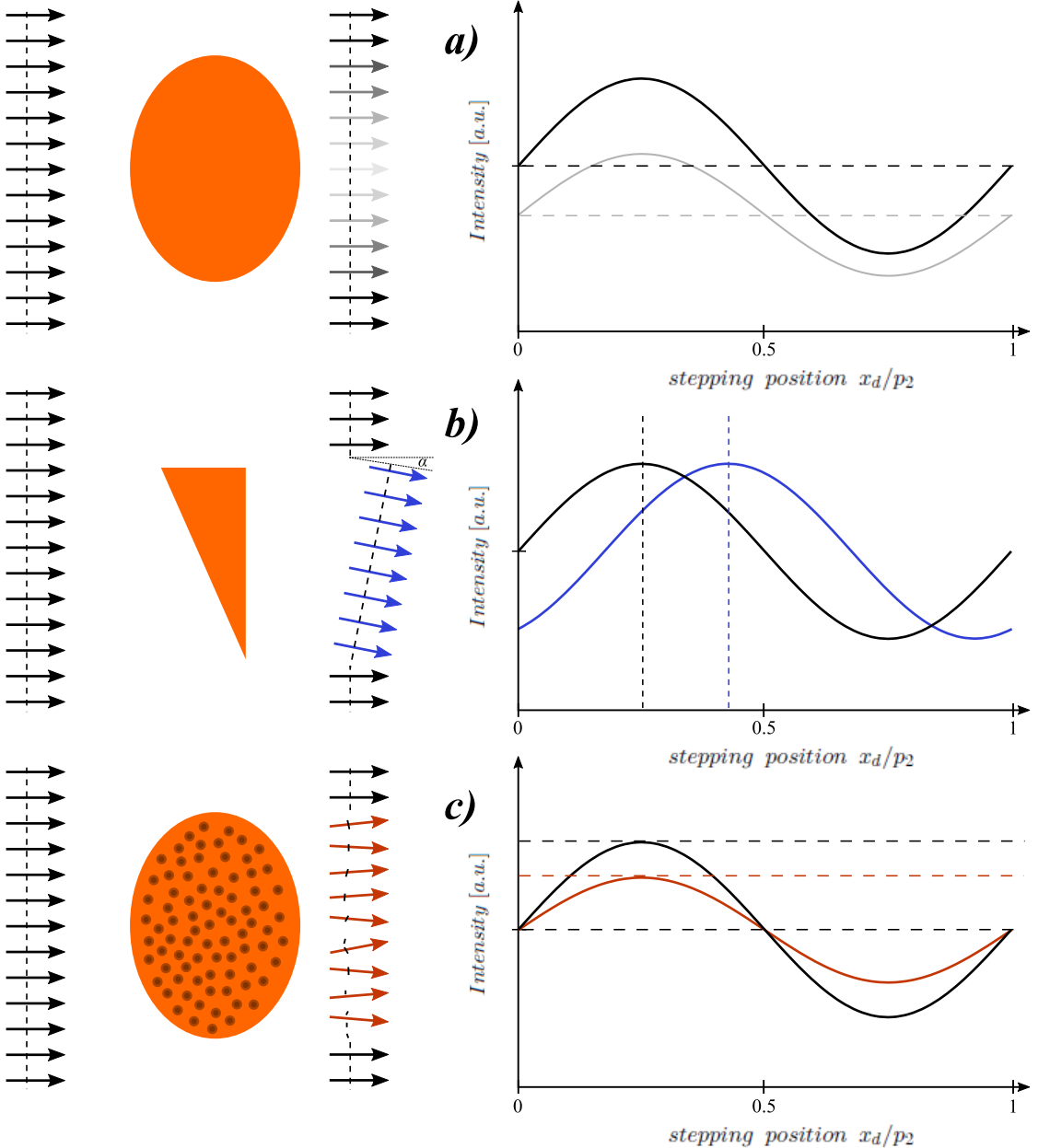


**Figure 2.6:** Resulting data output generated by the stepping procedure. The black solid line in the plots on the right side indicate the reference stepping curve, the coloured the curves including an object in the beam. a) the dashed lines indicate the respective mean intensity of the curve, so the decrease is proportional to the attenuation induced by the object. b) The transversal shift of the stepping curve is induced by a slightly deflection of the beam while passing through the object due to a differential phase shift of the incoming wave-front. c) due to small angle-scattering on sub-pixel features of the object the amplitude of the resulting stepping-curve is reduced.

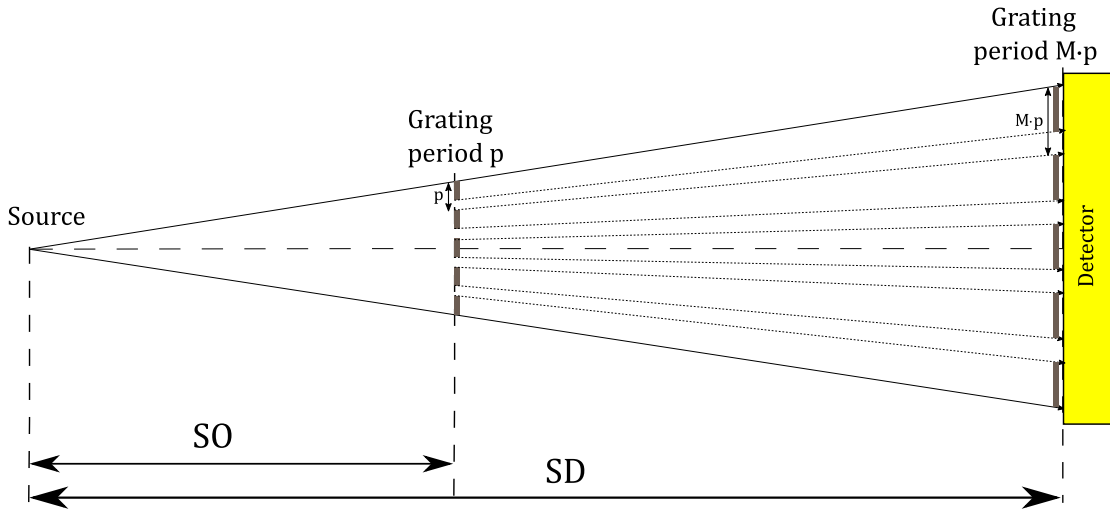


**Figure 2.7:** Geometric magnification in curved wave setups for a point like source. Depending on the position where the grating is placed in between source and detector the magnification factor varies from  $\lim_{SO \rightarrow 0} M \rightarrow \infty$  right behind the source, to  $\lim_{SO \rightarrow SD} M \rightarrow 1$  right in front of the detector.

gratings. These distances given by equation 2.13 also have to be rescaled in the manner that [4]:

$$d_{T_{frac}} = M \frac{np^2}{8\lambda}. \quad (2.31)$$

So the consequence of this effect is, that the geometry of the setup has to be considered before the production of gratings, which means that the same grating might not be usable for two different installations e.g. at one hand for a short setup in a lab and at the other hand at a synchrotron beam-line with a long geometry. In the next part another effect, arising from curved wave fronts and thus magnification, is discussed with respect to a measurement technique for the spot size of the source.

### 2.2.8 Induced uncertainty by an expanded edge thickness at different magnifications

Werd ich wahrscheinlich mit in die Auswertungen und Results packen. In the latter section the changes for the setup properties, arising by the transition from a idealized system to a more ‘realistic’ system, were induced, but there are some more changes, which have to be accounted for a real system. Since there is no real point source in nature, every source has an expanded shape, which leads to complexity characterizing such a system. One example is the measurement of the extent of the source spot, using a so called knife edge. Therefore the knife edge, speaking o a very sharp edge of a small metal cuboid, which has been polished to be as smooth as possible, is put right in the centre

of the beam. The exact procedure is described in chapter 5. In the following just the mismatch of this technique, with respect to the elongation of the edge in beam direction and the influence of the position of the ashlar speaking of the associated magnification, is considered. The relevant geometrical parameter for this are shown in Figure 2.8. Here denotes  $S/2$  the half of the expanded source size,  $M_\alpha$  and  $M_\beta$  the magnified image of the edge, whereby these two quantities differ from each other, corresponding to the thickness  $\Delta d$  of the ashlar and the angles  $\alpha$  and  $\beta$ , which are dependent on the position of the cuboid and the spot-size of the source, varying from each other in the same way like  $M_\alpha$  and  $M_\beta$ . For this case the tangent of  $\alpha$  and  $\beta$  is given by:

$$\left. \begin{aligned} \tan(\alpha) &= \frac{S}{2d} = \frac{M_\alpha}{l-d} \\ \tan(\beta) &= \frac{S}{2(d+\Delta d)} = \frac{M_\beta}{l-d-\Delta d} \end{aligned} \right\} \quad \frac{S}{2d} + \frac{S}{2(d+\Delta d)} = \frac{M_\alpha}{l-d} + \frac{M_\beta}{l-d-\Delta d}, \quad (2.32)$$

whereby the addition of both gives a relation between the spot size of the source and the magnified edge image resulting from the position between source and detector and the thickness of the ashlar. For the influence of the thickness  $\Delta d$  of the edge, just the equation for  $\tan(\beta)$  is of interest, because just for this half of the relation the extend of the ashlar comes into play, assuming that the whole X-rays are absorbed by the cuboid. Getting a feeling for the contribution of the thickness  $\Delta d$  the right side of the relation

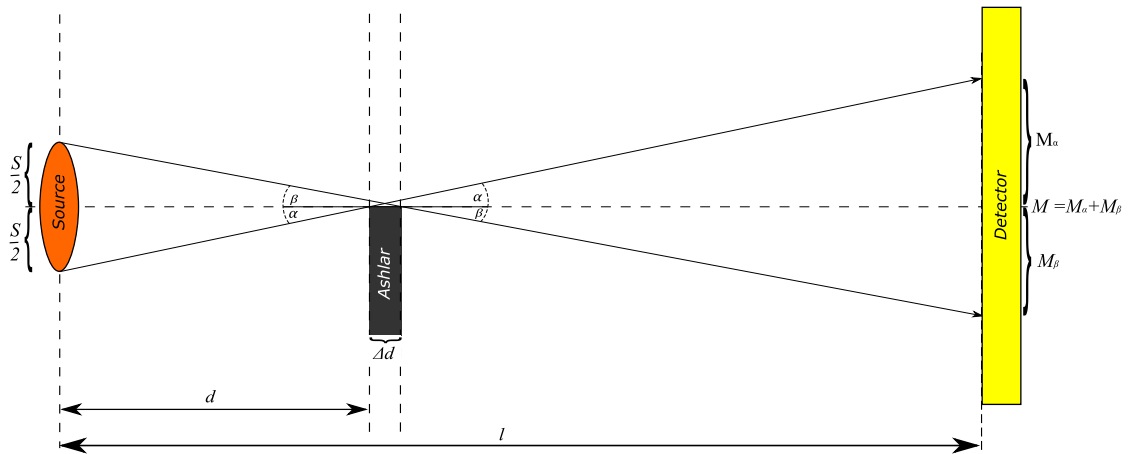


**Figure 2.8:** Sketch of the edge in the centre of the beam for the measurement of the source size. Due to the finite size of the edge in beam direction the upper half of the source produces a slightly smaller image of the edge on the detector-screen. This effect leads in reverse to a mismatch during the measurement of the size of the source.

from equation 2.32 for  $\tan(\beta)$  is rewritten with the first two terms of the corresponding Taylor expansion around  $d$  and  $(l - d)$ , respectively, whereby the small variation is the

thickness  $\Delta d$ . Thus  $\tan(\beta)$  becomes:

$$\begin{aligned} \tan(\beta) &\approx \frac{S}{2d} - \frac{S}{2d^2} \underbrace{(d - d_0)}_{\hat{=} \Delta d} + \frac{S}{2d^3} \underbrace{(d - d_0)^2}_{\hat{=} \Delta d^2} \\ \text{subst: } (l-d) &= x \\ \downarrow & \approx \frac{M_\beta}{x} - \frac{M_\beta}{x^2} \underbrace{(x - x_0)}_{\hat{=} \Delta d} + \frac{2M_\beta}{x^3} \underbrace{(x - x_0)^2}_{\hat{=} \Delta d^2}. \end{aligned} \quad (2.33)$$

As the focus lies on the contribution to the spot-size of the source, equation 2.32 is rearranged, so that the result is an expression for the source size :

$$S = \frac{d^3}{d^2 - \frac{d}{2}\Delta d + \Delta d^2} \left( \overbrace{\frac{M_\alpha + M_\beta}{x}}^M - \frac{M_\beta}{x^2} \Delta d + \frac{2M_\beta}{x^3} \Delta d^2 \right). \quad (2.34)$$

Getting a more manageable equation a substitution yields to

$$S = Ma - M_\beta(b - c), \quad (2.35)$$

whereby the substitutes  $a$ ,  $b$  and  $c$  replace the pre factor of the respective  $M$

$$a = \frac{d^3}{x(d^2 - \frac{d}{2}\Delta d + \Delta d^2)}, \quad b = \frac{d^3 \cdot \Delta d}{x^2(d^2 - \frac{d}{2}\Delta d + \Delta d^2)}, \quad c = \frac{2 \cdot d^3 \cdot \Delta d^2}{x^3(d^2 - \frac{d}{2}\Delta d + \Delta d^2)}. \quad (2.36)$$

As one can see is  $b$  and  $c$  a first and the second order term in  $\Delta d$ , respectively. Thus are these two the terms one is interested here, because the contribution to  $d^2$  of  $\Delta d \cdot d / 2 + \Delta d^2$  is negligible. For  $d = 0.5$  m and  $\Delta d = 0.01$  m, which are quite big values for both, and a complete setup length of  $l = 1.952$  m between source and detector, it is  $\approx -2.4 \times 10^{-3}$ , this yield to a value of  $a = 0.35$  m. The setup- length  $l$  is never changed during the whole measurement just the position o the edge in between. Getting a lower and upper appraisal, lower and upper values for  $d$ , and  $\Delta d$  are introduced, which are used in the latter measurement as well. The limits for  $d$  are set to  $d_{min} = 0.1$  m where the effect of the magnification is very strong ( $M = \approx 19.52$ ) and  $d_{max} = 0.5$  m. The thickness of the edge is never changed during the latter measurement, but at the first glance the focus lies on the influence of this property. So the limits for  $\Delta d$  are  $\Delta d_{min} = 0.005$  m and  $\Delta d_{max} = 0.01$  m. Here the subscripted  $max$  and  $min$  obviously denotes the maximal and minimal considered values. the different values of  $b$ ,  $c$  and  $(b - c)$  for different combinations of the limits are shown in Table:2.1. At the first glance it is obvious that just the influence of the first order-term  $b$  is yet very small. The contribution of the thickness  $\Delta d$  of the edge to this values has clearly a mathematical nature. Due to the small values the behaviour is strongly dependent on the enumerator, meaning that the half of the thickness halves the values for the linear term  $b$  and quarters them for the quadratic term  $c$ . Also One important aspect is, that the ashlar must have a distinct thickness, ensuring that as less as possible X-ray radiation passes through it, since in

other respects the sharpness in the image of the edge is reduced, and thus it becomes harder to determine the true source size. The contribution of the distance  $d$  between edge and source however changes the value about one order of magnitude, so regardless

	$d_{max}$	$\Delta d_{max}$	$d_{max}$	$\Delta d_{min}$	$d_{min}$	$\Delta d_{max}$	$d_{min}$	$\Delta d_{min}$
limits [m]	0.5	0.01	0.5	0.005	0.1	0.01	0.1	0.005
$b$	$2.4 \times 10^{-3}$		$1.2 \times 10^{-3}$		$3.0 \times 10^{-4}$		$1.5 \times 10^{-4}$	
$c$	$3.3 \times 10^{-5}$		$8.2 \times 10^{-6}$		$3.3 \times 10^{-6}$		$8.1 \times 10^{-7}$	
$(b - c)$	$2.4 \times 10^{-3}$		$1.2 \times 10^{-3}$		$3.0 \times 10^{-4}$		$1.5 \times 10^{-4}$	

**Table 2.1:** Results for the mismatch due to a finite edge thickness  $\Delta d$  and different magnifications. In accordance with mathematical relations the contribution of  $\Delta d$  to the values is strongly enumerator dependent, hence the small values. The second order pre factor term is always two times smaller than the first order pre factor term and thus negligible (No change of the value adding first and second order terms). Due to the small values of the first order pre factor which is always of the order  $\leq 10^{-3}$  the effect on the precision of the measurement can be ignored, since effects of misalignments of the edge deliver a much higher contribution.

of how thick the edge is the contribution of the magnification is higher of course just up to a distinct extent of the thickness, but no one would use a edge with a thickness of a few centimetres just because of difficulties aligning the edge perpendicular to the beam direction. The result of this evaluation is that the contribution of the thickness of the edge is negligible over a broad area, because even considering a unrealistic thickness of  $\Delta d = 10$  cm the pre factor  $b$  is just  $\approx 0.05$ . On the other side due to the bigger contribution of the magnification in this case it is more important insuring a preferably perpendicular alignment of the edge with respect to the beam direction, because a slight tilt of the edge induces a big smear o the image of the edge.

## 2.3 Spatial system response

In this section a short introduction to linear system theory is presented, focussing on the characterization of imaging systems. For a detailed insight the reader is referred to [7, 9, 21, 26, 27]. Here, only the basic quantities for the real and radially symmetric response functions are treated, representing the experimental setup, which has to be characterized.

### 2.3.1 Real- and frequency-space response functions

Linear system theory is a common approach describing the spatial properties of imaging systems. The applicability of the superposition principle on an imaging system implies it's linearity, meaning the response to a linear combination of input signals, is the same linear combination of the particular responses, called output signals. Assuming that the response of the linear system is also shift invariant, i.e. the system is linear and shift invariant (LSI), the output can be calculated by a convolution:

$$I(x, y) = S(x, y) \otimes O(x, y) = \int_{-\infty}^{\infty} \int_{-\infty}^{\infty} S(x - x', y - y') O(x', y') dx' dy', \quad (2.37)$$

$I(x, y)$  is the measured image,  $S(x, y)$  is the point spread function Point-spread-function (PSF),  $O(x, y)$  describes the object, and  $\otimes$  designates the two-dimensional convolution operator. Because of dealing with intensities, all functions in real space are real functions, therefore the PSF is defined to be normalized to unity, i.e.:

$$\int_{-\infty}^{\infty} \int_{-\infty}^{\infty} S(x, y) dx dy = 1. \quad (2.38)$$

For a full characterization of the spatial system response of a system, the measurement of the PSF or the appropriate Modulation transfer function (MTF) is absolute. The big advantage knowing these properties, is that they can be used correcting blur and other artefacts via deconvolution techniques. Since the PSF is the response of the system to a delta-peak shaped input signal, in other words the description of an image produced by a point-like source, which is inaccessible in real life, the PSF has to be derived indirectly from objects with well known structure like edges or slits. The related MTF can be expressed using the convolution theorem, stating that the convolution of two functions in real space is just a multiplication in Fourier space. Hence equation 2.37 becomes using convolution and Fourier transform

$$\mathcal{F}(I(x, y)) = \mathcal{F}(S(x, y)) \cdot \mathcal{F}(O(x, y)) \Rightarrow \tilde{I}(u, v) = \tilde{S}(u, v) \cdot \tilde{O}(u, v), \quad (2.39)$$

where the letters with tilde indicate the respective Fourier transformed function. The so called Optical transfer function (OTF) is the Fourier transform of the Point-spread-function  $\tilde{S}(u, v)$  and is in general a complex function, but can be split in phase and amplitude such as

$$\tilde{S}(u, v) = M(u, v) e^{i\Psi(u, v)}, \quad (2.40)$$

with the Phase transfer function (PTF)  $\Psi(u, v)$  and the so called Modulation transfer function of the system, related in a manner that

$$M(u, v) = \frac{|\tilde{S}(u, v)|}{\tilde{S}(0, 0)} = |\tilde{S}(u, v)| \quad (2.41)$$

is the absolute value of the OTF. This quantity correlates also with the reduction of contrast of an sinusoidal signal comparable to part 2.2.6. In general the PSF is assumed to be radial symmetric, thus a one-dimensional description in polar coordinates

is possible. Using this approach also the OTF is radial symmetric and thus real, which reduces equation 2.40 to  $\tilde{S}(w) = M(w)$  (whereby this is the polar coordinate representation which is still two-dimensional!). As consequence the system response can also be fully described by the MTF for this assumptions [9]. Now in the following sections the required mathematical armamentarium for the evaluation of the PSF from easy structured images is presented in a short manner.

### 2.3.2 Edge- and Line- spread function (ESF/LSF)

The spatial system response on an edge-shaped input signal is generally defined as the Edge spread function (ESF). On the other hand is the Line-spread-function (LSF) obviously the response on a line shaped signal. These functions are both two-dimensional functions, but with a constant behaviour along the direction parallel to the edge or rather line. According to this both can be expressed by a one-dimensional representation. In the further it is shown that the LSF is the first derivative of the ESF as well as the projection of the PSF. Considering that both objects are parallel to the y-axis, both functions are independent of y. Thus the Line-spread-function is defined as (using equation 2.37) [9]:

$$LSF(x) = \int_{-\infty}^{\infty} \int_{-\infty}^{\infty} S(x - x', y - y') \delta(x') dx' dy' = \int_{-\infty}^{\infty} S(x, y') dy', \quad (2.42)$$

with the Point-spread-function  $S(x, y)$  defined in section 2.3.1 and the Dirac-delta function  $\delta(x)$  describing the line object  $O_l(x, y)$  parallel to the y-axis, which is unity integrated from  $-\infty$  to  $\infty$ . Thus the projection of the Point-spread-function in y direction is equal to the  $LSF(x)$ . In contrast the edge object  $O_e(x, y)$  with the same constraints can be written as:

$$O_e(x, y) = O_e(x) = \begin{cases} 0 & \text{for } x \leq 0 \\ 1 & \text{else.} \end{cases} \quad (2.43)$$

Thus the ESF is given by [9]:

$$\begin{aligned} ESF(x) &= \int_{-\infty}^{\infty} \int_{-\infty}^{\infty} S(x - x', y - y') O_e(x') dx' dy' \\ &= \int_{-\infty}^{\infty} O_e(x') \int_{-\infty}^{\infty} S(x - x', y - y') \delta(x') dy' dx' = O_e(x) * LSF(x), \end{aligned} \quad (2.44)$$

here  $*$  denotes the one-dimensional convolution and  $O_e(x)$  denotes the function for the edge shaped object defined above. So the derivative of the ESF appears to be:

$$\frac{d}{dx} ESF(x) = \frac{d}{dx} \{O_e(x) * LSF(x)\} = \delta(x) * LSF(x) = LSF(x). \quad (2.45)$$

This equation holds because again convolution theory states, that the derivative of a convolution of two functions can be rewritten as the convolution of the derivative of one of the two functions with the other function or the other way round. In addition the derivative of the edge function results in the delta function, thus consequential the

derivative of the ESF yield to the LSF.

Furthermore it is possible to generalize the above defined relation, in order that the orientation of the edges or lines can be arbitrary only with one constraint, they have to pass through the coordinate origin. With that at hand it is possible to determine the two-dimensional PSF  $S(x, y)$ , using tomographic reconstruction techniques for edge projections with different angles. By assuming a radial symmetric Point-spread-function the Edge spread function (ESF) is independent of the projection angle and one edge is sufficient describing the full PSF. For further reading see [9].

### 2.3.3 PSF of a complex system

The former section describes the evaluation for the Point-spread-function (PSF) using edge or line objects. Now the determination of the PSF of a whole system is a very challenging problem, because each part e.g. source or detector of an imaging system has his own two-dimensional PSF. It is one problem to determine the Point-spread-function (PSF) of the whole system, but measuring this property is just one step towards the quantities, which are rather expected. The PSF of an simple imaging system, consisting just of source and detector, is given by convolution of the respective PSF's

$$PSF_{System} = PSF_{Source} \otimes PSF_{Detector} = \mathcal{F}^{-}[\mathcal{F}(PSF_{Source}) \cdot \mathcal{F}(PSF_{Detector})], \quad (2.46)$$

whereby the last part of the equation is just the first part, but rewritten in Fourier transforms to simplify the further explanations. In general one has to deal with a curved wave setup as explained in 2.2.7, thus due to geometrical thoughts one has to account the magnification in the latter equation, because the PSF of the source is spread out over the detector screen by this magnification factor. For convenience a one-dimensional behaviour is assumed for the further steps. Normally for X-ray sources a Gaussian shaped PSF is assumed, whereby the sigma (equal to the width of the function) of the Gaussian has to be multiplied by the magnification factor minus one, thus equation 2.46 is rewritten with Gaussian functions for the respective parts such that:

$$A_{System} e^{-\frac{1}{2}(\frac{x-b}{\sigma_{System}})^2} = \mathcal{F}^{-}[\mathcal{F}(A_{Source} e^{-\frac{1}{2}(\frac{x-b}{\sigma_s \cdot (M-1)})^2}) \cdot \mathcal{F}(A_{Detector} e^{-\frac{1}{2}(\frac{x-b}{\sigma_d})^2})], \quad (2.47)$$

with the amplitudes  $A_{System}$ ,  $A_{Source}$  and  $A_{Detector}$  and sigma's  $\sigma_{System}$ ,  $\sigma_s$  and  $\sigma_d$  for the different parts, respectively. The solution of this equation is straight forward, because the Fourier transform of a Gaussian is again a Gaussian, but with reciprocal width  $\sigma$ . With this equation at hand it is possible to determine the PSF of the source, by knowing the PSF of the detector, and thus the spot-size of the source which is general defined as the FWHM of this function. Hence the focus lies on the evaluation of the size of the source, special attention has to be given to the width of the respective Gaussian. For that reason some assumptions are made reaching this aim in a more easy way. Firstly the amplitudes are set to one and the offset  $b$  is set to zero, so the peak is centred around the origin. Then both sides are multiplied by the natural logarithmic function ln getting

rid of the exponential, so this yields to:

$$-\frac{1}{2} \left( \frac{x}{\sigma_{system}} \right)^2 = -\frac{1}{2} \left( \frac{x}{\sigma_s \cdot (M-1)} \right)^2 - \frac{1}{2} \left( \frac{x}{\sigma_d} \right)^2. \quad (2.48)$$

After cancelling out the pre factors and the  $x$ -es the equation simplifies to:

$$\left( \frac{1}{\sigma_{system}} \right)^2 = \left( \frac{1}{\sigma_{source} \cdot (M-1)} \right)^2 + \left( \frac{1}{\sigma_{detector}} \right)^2. \quad (2.49)$$

Inverting of the hole equation and taking the square-root the final equation for the system's spread width is given by:

$$\sigma_{system} = \sqrt{\sigma_{source}^2 \cdot (M-1)^2 + \sigma_{detector}^2}. \quad (2.50)$$

With this equation at hand it is now possible to determine the properties of a system at the spatial- and of course if needed at the frequency- domain.

### 3 The Setup

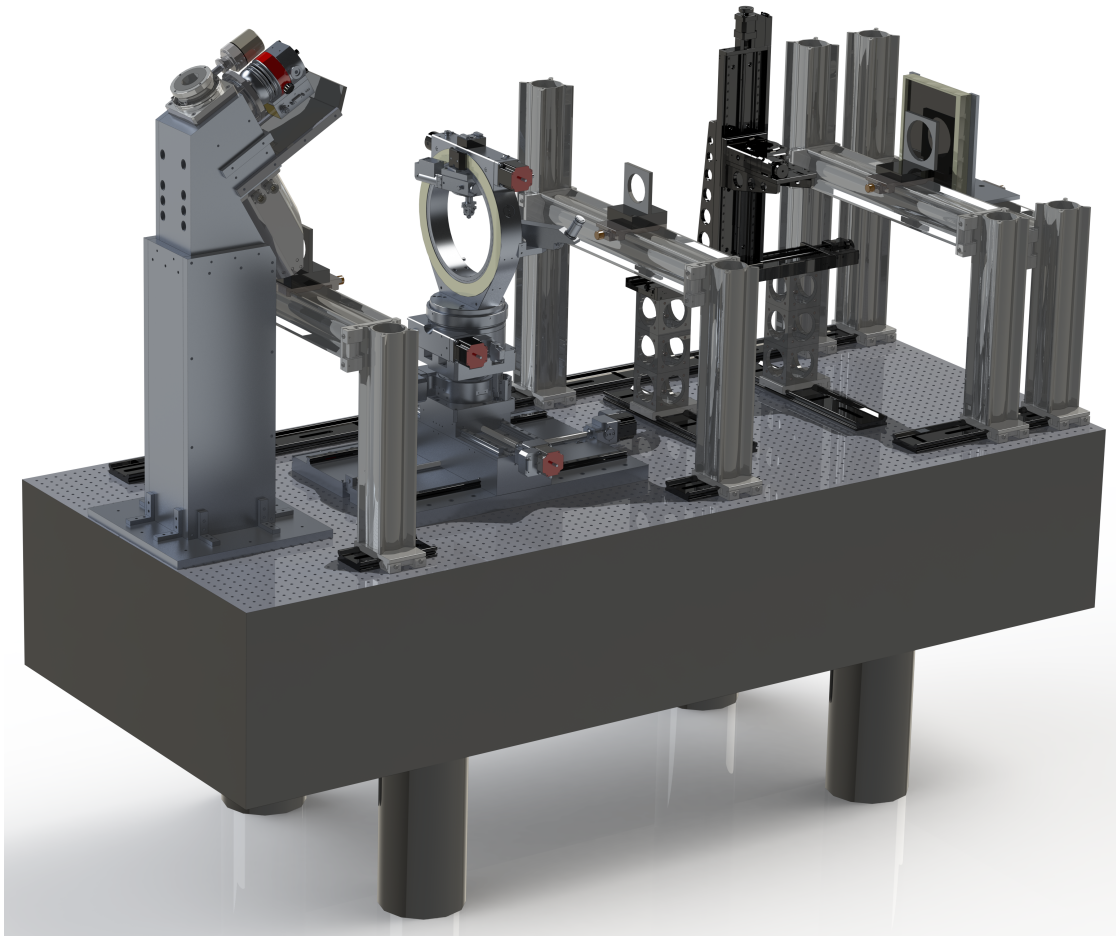


**Figure 3.1:** Rendering of the setup which is characterized in this thesis. The optical table has a size of  $2.4 \text{ m} \times 1 \text{ m}$ . On the left side the micro-focus X-ray tube and on the other side of the table the Varian X-ray detector is mounted, which is usually used for clinical applications. In-between the important part of this setup the grating interferometer with stages between the gratings, handling the samples during the measurements. (*courtesy by Friedrich Prade*)

In this chapter a short introduction is given, about the individual parts and their properties of the setup. The setup was built up in administration of the biomedical physics

group e17, by Friedrich Prade and Florian Schaff. The whole setup consists more or less of three main parts, Source, Interferometer and Detector. The general structure is depicted in Fig:3.1. The micro-focus source is placed on the left and the X-ray detector on the right side. In-between the part, which needs the most space and where the ‘physics’ happens, is mounted. Right in front of the Detector the analyser grating  $G_2$  is attached on its own bench, in the middle of the table the phase grating  $G_1$  is also placed on a bench, and right in front of the source the so called source grating  $G_0$  is mounted. All gratings are preferably aligned perpendicular to the beam direction and with the same orientation of the grating-lines to each other, avoiding shadowing and that Moire-fringes show up. Between the gratings two different stages are placed handling the samples during the measurement, which can be controlled fully automatic, thus computer tomography measurements without interrupting the procedure are possible. In the next three sections the different parts are highlighted in a more detailed way, starting at the very beginning, the production of X-rays at the source, followed by the interacting part within the interferometer and at least the creation of the images at the detector.

## 3.1 The source

The most indispensable part is of course the production of the required radiation itself. At this setup a so called ‘micro-focus’ X-ray tube designed and crafted by ‘X-RAY WorX GmbH’ is used, which provides some big improvements compared to commercial X-ray sources used for clinical applications, especially at the area of resolution restraints. The structure is in general like the structure of a conventional x-ray tube, but with additional parts e.g. an electron optic influencing the direction of the electrons generated by the cathode. For a complete overview of the properties and drawings of micro-focus tubes provided by this company see [30, 31, 32, 33].

### 3.1.1 Dimensions and structure

The dimension and structure of the source differs just in the additional parts from conventional sources. It consists of a cathode filament heated by a high voltage power supply generating a electron beam, which is accelerated due to a electromagnetic field between cathode and anode, to the other end of the tube hitting a tungsten reflection target, which finally produces the X-ray radiation. In-between of these two main parts a additional part, a so called electron optic is placed. It consists of several magnetic coils which influences the trajectory of the electron beam. Four coils are responsible for the deflection of the whole beam in both x and y direction. The other coils are used focussing the electron beam, which is in general spread over a large area, to a very tiny area improving the resolution strength of the whole setup. A drawing of the dimension of the source and the electron optic in detail is shown in Fig. 3.2. Using such a focussing equipment, it is inevitable to evacuate the whole tube avoiding flash-overs between filament and target. This is possible, because due to the strong compression of the particular electrons in the beam a ‘electron bridge’ guiding current from cathode to

anode can arise. Therefore in addition a vacuum turbo pump is mounted on top of the tube, providing a vacuum of the order of  $1.5 \times 10^{-6}$  avoiding such flash-overs. As in conventional sources just about one percent of the electrons hitting the target, produces X-ray radiation. The remaining part heats the anode material. Thus especial for the case of a focussing source a cooling of the target is needed, avoiding that the target material melts down.

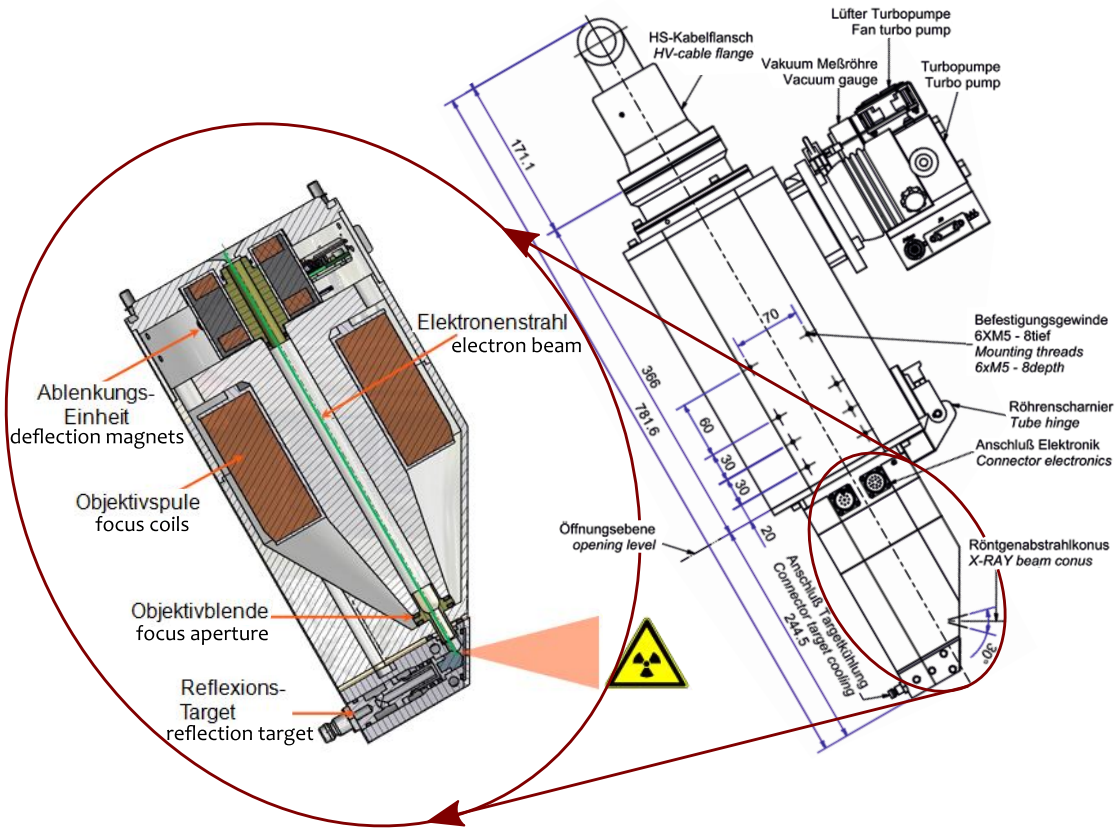


**Figure 3.2:** Dimensions of the source and its components. The part highlighted in the red circle shows the focussing electron-objective, which improves the final resolution due to the fact scaling the spot size down to the micron range. The upper part of the electron optic consists of deflection magnets for the x-y plane. Subsequent to this are the focussing coils placed, which collimate the electron beam, denoted by the thin green line, to reach a really small impact point at the target. (source: ©X-RAY WorX GmbH 2015 <http://www.x-ray-worx.com>)

### 3.1.2 properties

In difference to conventional X-ray tubes this tube is working over a broad tunable range from 20 kV up to 160 kV, but due to the design energy of the Talbot-Lau interferometer it

operates in general at 60 kV. Depending on the adjusted acceleration voltage the power-output ranges from 1 W up to 300 W. The construction of the tube offers a almost infinite lifetime, because the filament, which is the only thing which usually breaks down, can be easily changed, thanks to its ‘open’ architecture (see Fig.3.2 right behind the opening level the filament holder is mounted). Another advantage compared to conventional sources with a spot size of  $\approx 2 \text{ mm}^2$  is that the spot size of this source is reduced down to the micron range. Hence the spatial resolution is strongly improved, why it is possible resolving features down to sizes of  $\approx 2 \mu\text{m}$  [33]. With the X-COM software [32] also developed and traded by X-RAY WorX several adjustments are possible. One example for an additional feature is the possibility to ‘stepp’ the beam in both x or y direction thanks to the linkage of the deflection magnets. With this feature a transition from a mechanical stepping procedure to a ‘magneto-stepping’ for the phase contrast technique comes into range, which provides several advantages e.g. prevention of grating vibrations during the stepping process.

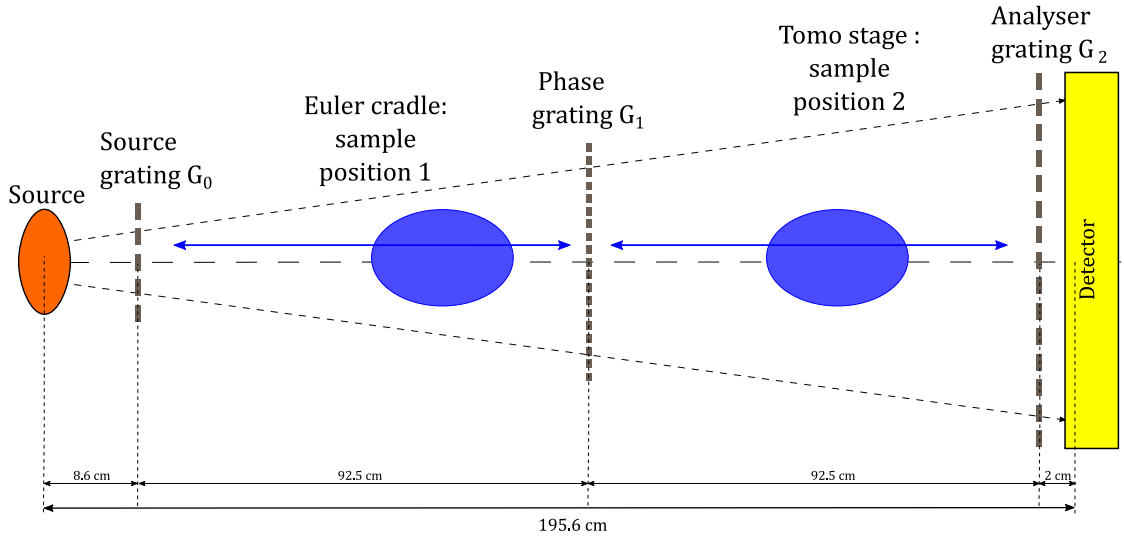


**Figure 3.3:** Drawing of the relative distances in-between the setup and different sample positions. This drawing shows a symmetric setting of the gratings, thus the magnification factor is 2 and the analyser grating has twice the periodicity as the  $\pi/2$  phase grating. The gratings are also arranged to operate at the first fractional Talbot distance. The blue extended arrows indicate the possible positions for the sample between the gratings.

## 3.2 Sample handling between the gratings

As depicted in Fig.3.3, the Talbot-Lau interferometer itself captures the main part of the setup length, starting about eight cm behind the source, with the source grating  $G_0$ , which is an absorption type with a grating period of  $10 \mu\text{m}$  and a height of  $150 \mu\text{m}$ .

At the other side just two cm in front of the flat-panel detector the analyser grating  $G_2$  with the same periodicity of  $10\ \mu\text{m}$  as  $G_0$  and a grating height of  $160 - 170\ \mu\text{m}$ , thus also and absorption grating, is placed. Due to the high absorbency and the easy handling these two gratings are made of gold as described in 2.2.4. Accounting the magnification factor of two for a symmetric setup, the phase grating  $G_1$  with a periodicity of  $5\ \mu\text{m}$  and a nickel height of  $8\ \mu\text{m}$  has to be put right in the middle between the other gratings so the distance between the gratings is generally  $92.5\ \text{cm}$ , respectively. The gratings are not set arbitrarily to these distances, but they are put there on purpose, accounting the first fractional Talbot distance for a design energy of  $45\ \text{keV}$ . In-between the gratings two different kinds of sample holders are placed with different properties. The first one between  $G_0$  and  $G_1$  is an Euler cradle. the main advantage of this stage is, that the sample can be rotated around its own axis and furthermore rotated around the beam axis as well. The second stage is a usual tomography stage which is put between  $G_1$  and  $G_2$ . Depending on the expected results and the sample is put on one of these two stages. So as example if a bigger magnification is needed resolving small detail within a sample the Euler cradle is recommended. On the other hand if one is interested in the induced phase shift one has to assure to get close to the phase grating, because the sensitivity enhances getting closer to it. But for this case both stages are feasible, because it makes no difference if the sample is placed in front or behind the phase grating.

### 3.3 detector properties

The detector used for imaging is a PaxScan 2520 DX digital flat-panel detector generally used for dental cases. The detector is developed and traded by Varian medical systems and is based on amorphous silicon technology with Caesium Iodine (CsI) as conversion material on top. The main advantage of this material are radiation hardness  $> 1\text{Mrad}$ , a broad input energy range from about  $40 - 160\ \text{kVp}$ , good low dose performance, immunity for single photon events within the substrate and proven 3-D soft tissue capability. The total pixel area is  $19.5 \times 24.4\ \text{cm}$  with a pixel size of  $127\ \mu\text{m}^2$  this yields to  $1536 \times 1920$  pixel. The limiting resolution is stated to be  $3.94\ \text{lp/mm}$  or in other words  $253.81\ \mu\text{m}$  in both x- and y-direction [23]. A picture of the detector is shown in Fig.???. For reasons of protection a  $2.5\ \text{mm}$  thick carbon fibre plate combined with aluminium is placed in front of the active detector area. Right behind this plate the active crystal layer with  $\approx 9\text{mm}$  thickness is placed.



# 4 Time- and power-stability of the X-ray tube

The following chapter contains the characterization of the time- and power stability properties of the source used at this setup. This qualities are elemental, getting a feeling about the performance of the source. For example a fluctuation in the radiation-output during a measurement can destroy the whole outcome, because e.g. a correction with a flatfield does not properly cancel out the influence of the source-spectrum during the measurement.

## 4.1 Time-stability

First of all the time performance of the source is examined in a more detailed way, to have a first impression how stable is the performance of source-output. Therefore a fist measurement of the influence of the exposure time onto the detector response is done, which is usually assumed to be linear for a integrating detector. Knowing this dependency, it is possible to compare images with different exposure-time, but the same X-ray energy and input-power. For example one image is taken with 5 seconds exposure-time and the other with 10 seconds, one can compare them by simple multiplication or division of the intensity in one image with the difference time-factor of the two images, for this case also by a factor of 2. This knowledge is very helpful, because especially in material research the dose is not the limiting factor and one can spare a lot of measurement time. *weiß nicht ob das so gut als Beispiel passt* The dependency of the detector used for this thesis is shown in Fig: 4.1. At the left side the dependency is shown in a plot with linear scaled axes. For better insight onto the variations the same data are plotted as well on the right side on double logarithmic scaled axes. Obviously is the behaviour on the left side as well as on the right side really linear, which is very positive for the further characterization. Furthermore show these plots already a first advice onto the stability of the source-output, because fluctuations within the source intensity, would destroy the linear behaviour.

**Long- time stability** As a next step the long time behaviour of the source is examined in more detail. This property is of big importance e.g for tomographic measurements, because they are very time extensive. The main problem of a variation of the source intensity for this case is, that due to this artefacts are induced in the latter tomographic reconstruction. If the intensity e.g. drops down during the measurement the first projections have better statistics and are brighter, than the projections at the end. Therefore

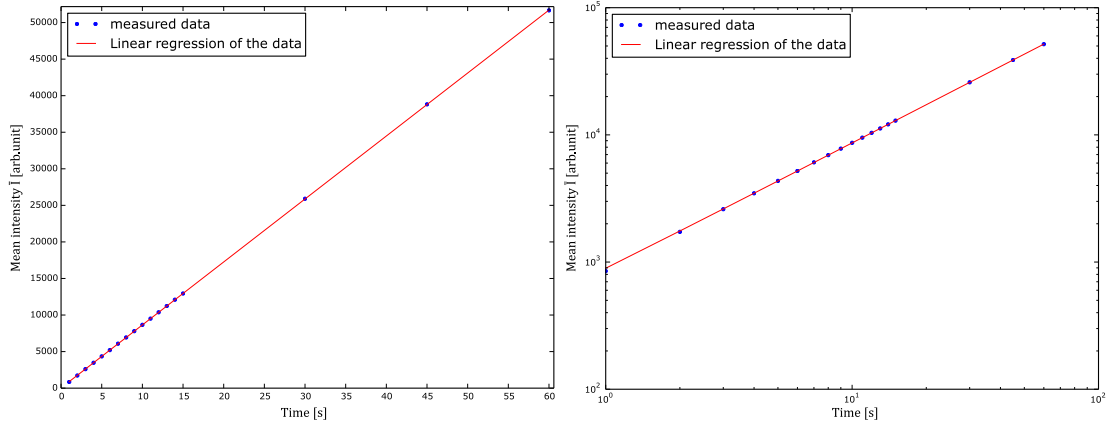


**Figure 4.1:** Dependency between the detector response onto a steady source output intensity during different exposure times. The left plot shows the measured data points and the corresponding linear regression on linearly scaled axes. The right plot illustrates the same data and their regression, but on a double logarithmic scale. The big benefit of this plot is, that variations within the recorded intensity have much more influence on the logarithmic scale than on a linear one.

usually flat-field images are taken in between the respective projection blocks. A flat-field image is a picture without any sample, so just the pure source-intensity distribution is recorded. The projection images are then afterwards corrected by division with these flat-fields to avoid the influence of the intensity drop. As one can imagine, the frequency taking such flat-fields is again a trade off between time effort and precision. So for the case that the time behaviour of the source is well-known one can e.g. adjust the frequency of the flat-fields, but regardless of the respective measurement technique the stable the source the better. For the determination of the time-stability of the source used for this thesis a phase tomography data-set recorded of Friedrich Prade is taken. The complete measurement time was around two days and within these two days every 20 minutes a block of stepped flat-fields is taken to correct the projection images. With the stepping routine described in 2.2.6 one can retrieve the corresponding mean intensity and the visibility, whereby the mean intensity is just the parameter  $a_0$  within a region of the image without any gratings. The Values for this two parameters are depicted in Fig:4.2. The left side shows the mean intensity averaged over three sections of the images without gratings, and the right side shows the mean visibility without any sample. The variation of the intensity varies with respect to the start value around  $\approx 1\%$  which is on this time scale very low and with disregarding the spike at about 2.5 hours the variation is even lower of  $\approx 7\%$ . The change of the visibility during the measurement time of  $\approx 4.5\%$  is a bit higher with respect to the start value of 21,35 % but still in a good region.

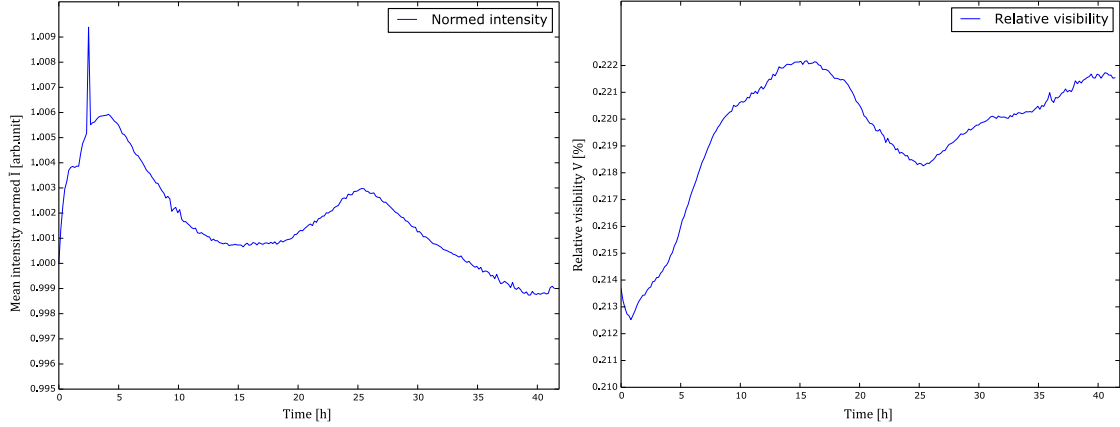


**Figure 4.2:** Time stability of the source in between two days. The left side shows the fluctuation of the mean intensity during the measurement, the right side shows the corresponding visibility. The data points are extracted from the flat-fields taken between two projection blocks. The variation over the time is in both cases very small. The mean intensity varies  $\approx 1\%$  which is very low and also the visibility varies just about  $\approx 4.5\%$  compared to the start value, respectively.

## 4.2 Power-stability

After the determination of the time-stability of the source also the power-stability is an important property, which is worth to be characterized. The procedure is a very easy one. In this case the energy and the exposure time is fixed to a distinct value for this case the energy of the electrons is set to 60 keV and the exposure time is for the first measurement set to 10 and for the second to 5 seconds, respectively. With the linear behaviour discovered in the latter section, the second data are multiplied by a factor of two for a better comparison. Tuning the power of the source by a fixed energy results in a change of the emission current of the filament, which results in more or less emitted electrons producing X-rays. The behaviour of the function  $P[W] = U \cdot I$  with a fixed  $U$  and the constant electron charge  $e$ , should result in a more or less linear function, but the main interest of this measurement lies on the resulting intensity of the X-rays instead of directly measuring the applied current. The plot in Fig:4.3 shows therefore the intensity averaged over the centre of the recorded image versus the power. As mentioned above, there are two measurements with a time delay of about half a year, double checking the dependency and especially the drop of the intensity in all four curves at about 25 – 40 Watt. In each measurement, the mean intensity is measured one time with the usual gratings inside the beam and one time without them. Hence, also the pure attenuation due to absorption of the grating materials is explored. As one can see the two curves with gratings lie over the whole power range always close together, whereupon the both without gratings differ more and more during the measurement.

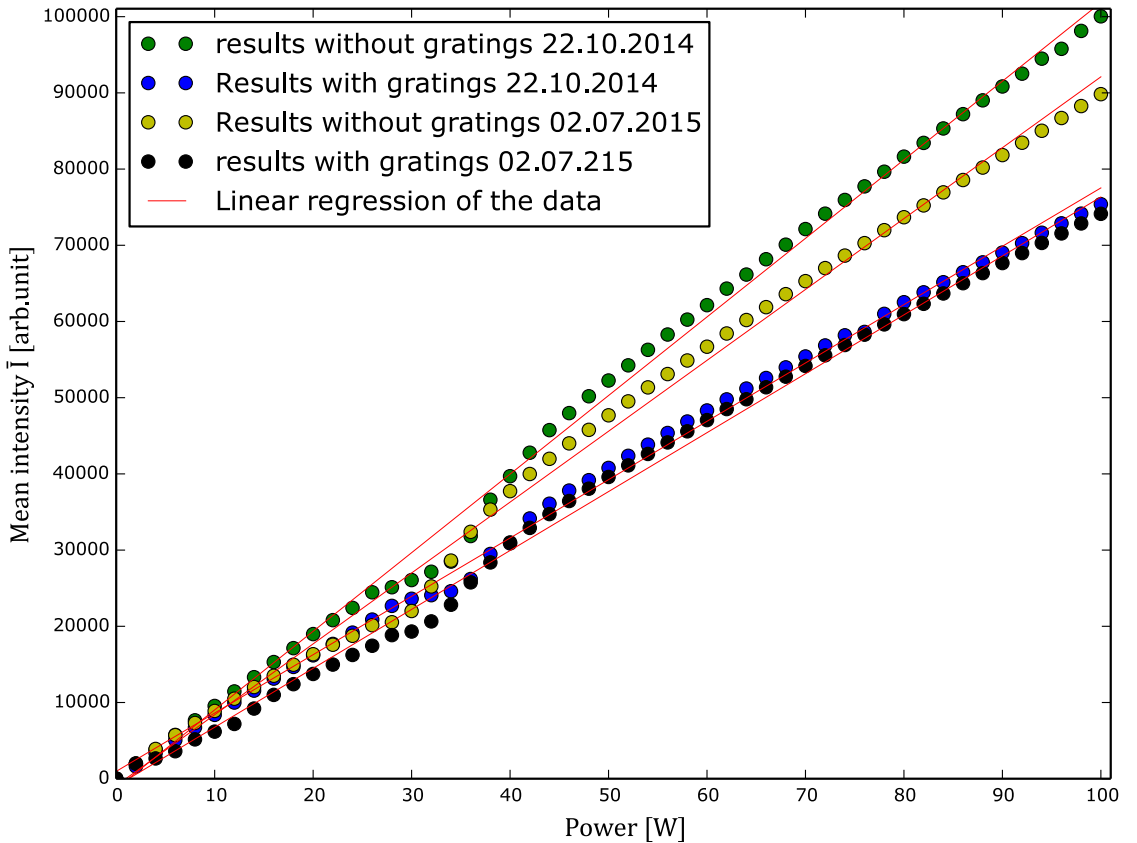


**Figure 4.3:** Behaviour of the power-stability of the source for a fixed energy at 60 kV. The plot shows four different data sets for two different dates. The Two sets marked with blue and black dots show the source behaviour with gratings in the beam, the two with yellow and green dots without anything inside the beam.

One possible explanation for this is, that due to the confined lifetime of the filament one measurement took place at the end of such a period, so there were less X-ray photons produced. Another explanation is a small change in the source spectrum, because the loss of intensity is just distinguishable in the case without gratings. This means that the spectrum for the latter measurement was possibly shifted to slightly lower photon energies, because lower photons contribute less to the intensity than high energy. This is also in accordance to the curves with gratings, because photons with lower energy are almost completely absorbed in the grating material and have thus for both measurements no contribution to the intensity within the image. As one can see is the drop at 25 – 40 Watt no measurement error, but rather an intrinsic source property. The explanation lies within the electron optic of the source. As mentioned in section 3.1.1 and shown in Fig:3.2 this optic focusses the electron beam down to a very small area. But this is

just possible for a distinct power range, because otherwise would the target be severely damaged by the deposition of too much heat on a too small area. Hence, the focus coils have to open up. Unfortunately this is not happening smoothly but rather at a distinct power for this case at 25 Watt. After this the impact area on the target increases rapidly until a distinct point. A side-effect of this is a loss of intensity, because more electrons just deposit their energy in terms of heat within the target material. *ist glaub ich nicht so ganz richtig*

**Conclusion** In summary one can say, that the performance of the source is for both cases in time- as well in power-stability in a good position. Of course is the variation in time and power influenced by several internal and external factors, but these results give a good rule of thumb improving the future measurements. Maybe they can even explain some artefacts in the recorded images or one can improve with this the image quality and also shorten the expenditure of time. For example in the flat-field case it is senseless to take a flat-field after one or two projections if the source is stable for a longer time period. *hier muss noch mehr hin einfach alles nochmal zusammenfassen?*



# 5 Characterization of the spatial system response

## 5.1 Knife edge measurements

In this section the acquisition of the data and the resulting outcome for the measurements with a knife edge is presented. At the end of the chapter a comparison between this technique and the one presented in section 5.2 is given.

### 5.1.1 Data acquisition

The characterization of the response of a system can be described in the spatial domain as well as in the frequency domain, but of course with the Fourier transform the transition between these two spaces is very easy. This section therefore focusses only on the spatial domain, because the main interest lies on the determination of the source size in different directions. There are several methods to determine the spot size of the source e.g. with thin slits, rods or pin-holes etc. For a detailed overview about the different methods and corresponding norms see: [3] or EN,ASTM,IEC. The most common way to determine this property is to use a sharp edge, which is projected onto the detector screen. This projected edge-profile is also known as the ESF described in section 2.3.2. A image of such a sharp edge and their corresponding projection is shown in Figure 5.1. a) shows the projection image of the edge, which was taken at a photon energy of 60 keV, a power of 80 W and with a magnification of 24.45. As one can clearly see is the edge smeared out over several pixels, due to the geometrical unsharpness induced by the limited spot size. b) shows the edge which has a polished side to smooth the surface and hence improve the sharpness of the edge. To reinforce the contrast in the projection image, the cuboid containing the edge has a thickness of 5 mm and is made of stainless steel, because of its good absorption properties up to high photon-energies and the possibility to easily polish the surface. Usually the thickness of such edges is thinner, because the thinner the edge the less the influence of a misalignment of the edge onto the measurement. But as shown in section 2.2.8 the influence of the edge-thickness is negligible over a broad range, preconditioned that the edge is positioned perpendicular to the beam.

**Edge alignment** To fulfil this condition the edge is positioned on the Euler-cradle and first aligned by hand to be perpendicular to the beam. After that the centre of the beam on the detector screen is determined with a small python script. To adjust the edge as perpendicular to the beam as possible, the edge is at first positioned at a certain distance apart from the source right in the centre of the beam. After that the edge is rotated

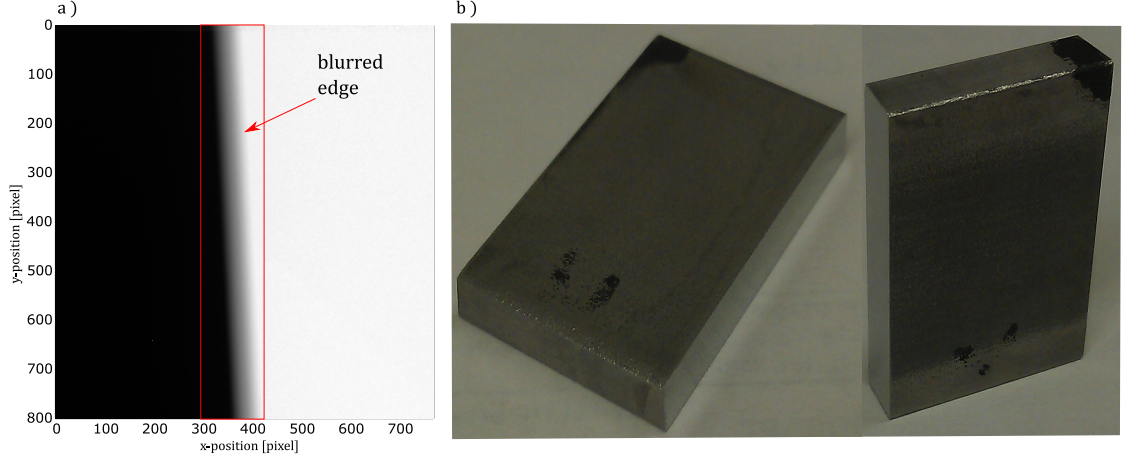


**Figure 5.1:** a) Image of a projected edge required of the detector. The edge is slightly tilted ( $\approx 3^\circ$ ) for the images to provide afterwards at the data-processing a sub-pixel resolution. b) Two pictures of the cuboid with the edge profile on two opposite sides. The two thin sides of the cuboid are polished, to get a smoother surface and thus a sharper edge.

around its own y-axis. Hence, the edge is on purpose misaligned in certain angle steps with respect to the z-axis. At each of these angles a image is taken and corrected with a flat-field. Afterwards the projection images, comparable to Figure 5.1 a), are projected onto the plane perpendicular to the edge to improve the statistic and reduce the image noise. This procedure is comparable with a line-plot over each pixel row and a subsequent averaging over all pixel rows. This projection of the edge shows the intensity variation between the different pixels. Such a projection of the edge-profile or the corresponding ESF is shown at the top of Figure 5.4. The shape of the profile reminds to a blurred step function. This shape can be roughly split in three parts. One part which has no intensity, because inside the cuboid the X-rays are almost completely absorbed. Another part with high intensity in each pixel, because no absorbing material is inside the beam. These two parts lead to a horizontal line, because the neighbouring pixels have the same intensity values, but of course with antithetic values. Finally the third part right in between the other parts, which is the projection of the edge itself. There the shape of the projection is an increasing or decreasing line (depending on the projection direction), with a more or less steep slope, which is correlated to the geometrical unsharpness and the misalignment of the edge. On this shape a error-function is fitted to get parameters for the comparison of the different ESFs. Since the best angle corresponds to the steepest ESF, the slope of the fit-functions is plotted against the different angles. **do here the processing of the edge alignment generating such a plot** This results in a parabola, whereby the vertex of the parabola indicates the best edge position. If the edge was well aligned in the first place the value of the best angle should be near start value. This procedure is at first done in rough steps likewise in both directions around the start

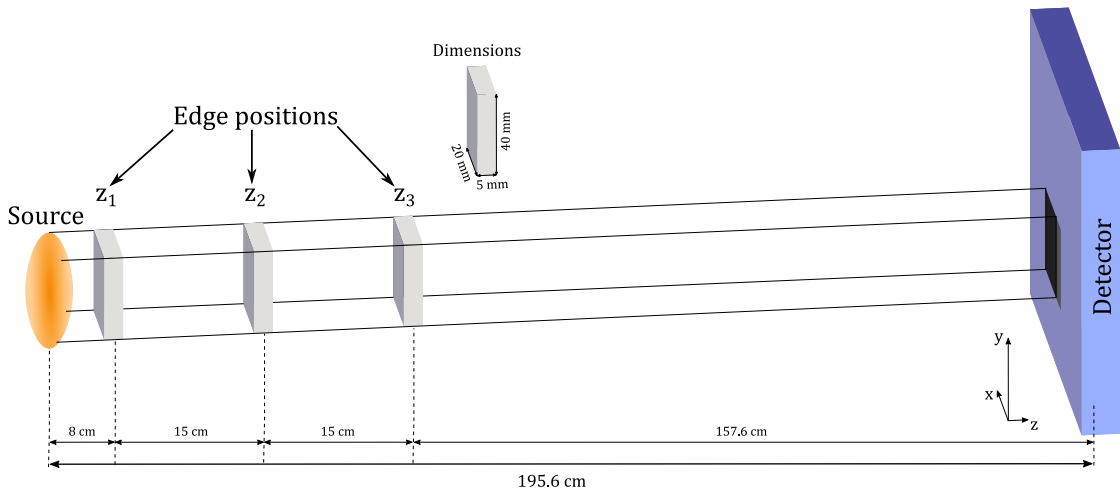


**Figure 5.2:** Illustration of the different edge positions during the measurement. Due to magnification the projection of the edge is spread over the detector plain perpendicular to the edge direction. The edge is placed on the Euler cradle, which is not shown here. To get a easier insight of the different arrangements a small coordinate system is placed right in front of the detector screen.

angle and afterwards with finer steps around the best value of the first measurement.

**Measurement procedure** After adjustment of the edge, the main measurement starts. Therefore the edge is measured at three different distances with respect to the source. Usually one distance is sufficient for the determination of the PSF and the corresponding spot size, but with three different distances the exploration of the influence of the magnification onto the measurement results is possible. The different distances are chosen to be close to the source plane to reduce the influence of the detector PSF and also to get a sufficient magnification of the edge resolving the spot-size of the source. This need showed up, because during the first measurements the determination neither of the PSF nor of the spot size was possible, since the pixels and the PSF of the flat-panel detector are to big. The distances and the cuboid dimensions for the measurement are exhibited in Figure 5.2. The distance between the different positions is equidistantly set to 15 cm, at one hand for reasons of simplicity and at the other because the Euler-cradle has also a limited traverse paths in every direction. The edge is at first slightly tilted around  $\approx 3^\circ$  at the z-axes (cf. Figure 5.1 a)), to provide a better resolution for the projection of the edge-profile. At each of the particular z-positions a flat-field is taken. Afterwards the edge is placed in three different directions in the beam, one vertical, the second horizontal and the third at the bisecting line of the first two positions, around the z-axis. After a short waiting time, to decrease vibrations induced by the driving around of the Euler-cradle, an image at each particular position is taken. With this approach it is pos-

sible to determine the shape of the spot-size and also the rotation of the source-shape in the x-y-plane at once. Thanks to the possibility to control every stage in the setup from outside, only the adjustment on the sample holder of the Euler-cradle is necessary and the measurement itself is done automatically using a control script, containing the different positions and parameter. This measurement is done for three different energies at 40, 60 and 80 kV and thereby repeated in feasible steps over the whole power range. This implies e.g. for a photon energy of 60 kVp a range of 160 Watt, leading to over 50 measurements, whereby every measurement contains 9 projection images and three flat-fields (one for each z-position). With this images at hand, the determination of the PSF of the system is possible, but for the determination of the source-size an additional measurement is needed.

To evaluate the source size, also the PSF of the Detector has to be determined. As mentioned in section 2.3.3 are the results of the described measurement above the convolution of the source and the detector, PSF respectively. The approach is very similar to the upper case, but also much less time extensive. To determine the PSF of the detector, the same edge is placed right in front of the detector plane. With this it is made sure that the influence of the source is negligible, because the PSF of the source scales with a factor of  $M - 1$  and for the position of the edge right in front of the detector the magnification is in good approximation unity. The edge is placed again in vertical as well as in horizontal direction, but due to the lack of a feasible sample holder a measurement diagonally to the pixel was not possible. But this problem can be easily solved during the processing by quadratic addition of the vertical and horizontal value to get a measure for the diagonal PSF as explained in the next section. This measurement is also repeated for the different energies, because the PSF of the detector can not necessarily be expected to be constant for different energies.

### **5.1.2 Data processing**

For reasons of simplicity, this section just considers the processing of a data-set of one energy, in this case the one for 60 kV, because the treatment of the data-sets is for every energy the same, disregarding some changes in the projection angle or some computing parameters. To get the information out of the projected edge-profiles, the images are at first corrected with the corresponding flat-field. After that a rectangular section of about  $250 \times 250$  pixel, which only contains the blurred edge, is cut out of the images to reduce computing time. This section is then projected perpendicular to the edge direction (cf. Figure 5.3), to get a ESF with a good statistic. To assure that the projection is accurately done to the plane perpendicular to the edge, the same procedure as in section 5.1.1 (edge alignment) is followed, with the difference that here the projector gets on purpose wrong projection angles. For this determination one image of the whole data set with a vertical oriented edge is sufficient, because the angles for the other projection directions are correlated to each other due to the Euler cradle and can be adjusted by simply adding  $90^\circ$  for the horizontal case or  $45^\circ$  for the diagonal case, to the projector angle. For this data-set a image of a nearly vertical edge at the second measurement

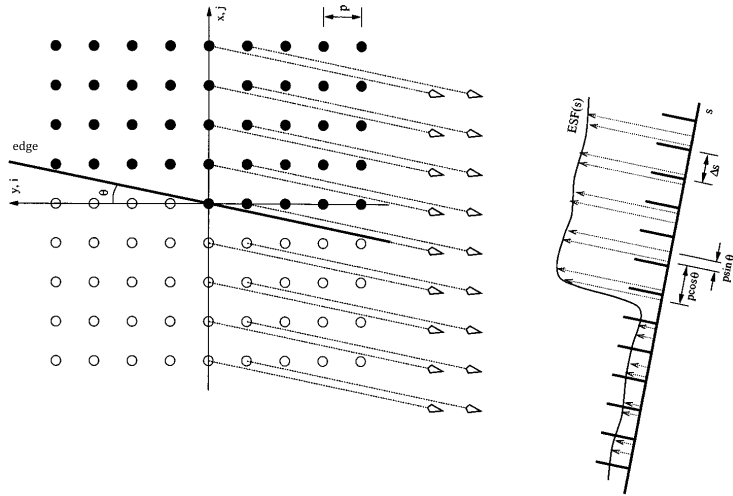


**Figure 5.3:** Projection of a tilted edge onto a plane perpendicular to the edge direction. Each pixel is projected under the same angle onto the projection plane. With this technique the two dimensional edge image is reduced to a one-dimensional trace known as the ESF. (adapted from [21])

position ( $z_2$ ) with a power of 80 Watt is chosen. With the projection angle found by this analysis, the whole data-set is projected afterwards. As mentioned above, the edge is slightly tilted from the usual coordinate axes. Using this treatment it is possible to get a sub-pixel resolution in the projected image, because the projector can split in this case each pixel by a certain number of sub-pixels and thus enhance resolution of the ESF. The splitting of one pixel in several sub-pixel is just accurately possible with a tilted edge, because every possible shadowing setting of a detector pixel occurs. In contrast to that, for a edge exactly vertically aligned to the pixel rows only three possible shadowing settings occur, either the edge covers the whole pixel, the edge do not cover the pixel, or the edge is somewhere in the middle of the pixel.

To facilitate the further steps the ESF is normed between zero and one. On this normed ESF again an error-function is fitted. As shown in section 2.3.2 is the LSF the first derivative of the ESF and in this case the first derivative of an error-function results in a Gaussian-function. For that reason the parameter of the error-functions can be taken to fit the PSF of the system. To get a better imagination what happens at the particular processing steps Figure 5.4 shows some results for the error-function fit and the Gaussian fit. The plots show the results for the case of a vertical edge at an energy of 60 kV and a power of 80 W, for the different edge distances. The top plot shows the ESF with the corresponding fit of the error-function, and the plot below the related Gaussian fits. As one can clearly see is the influence of the magnification onto the width tremendous, but after correction with the respective factor the three curves should have the same width. As suggested in the latter section for the determination of the source size also the PSF of

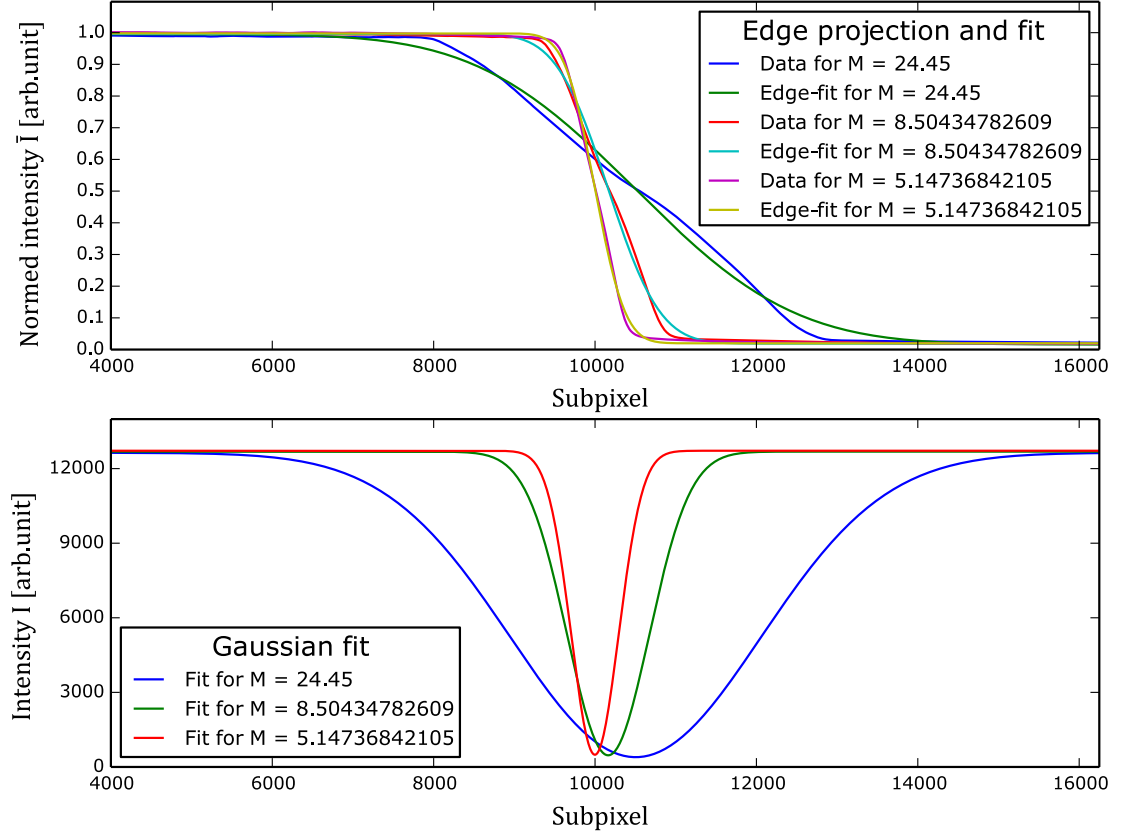
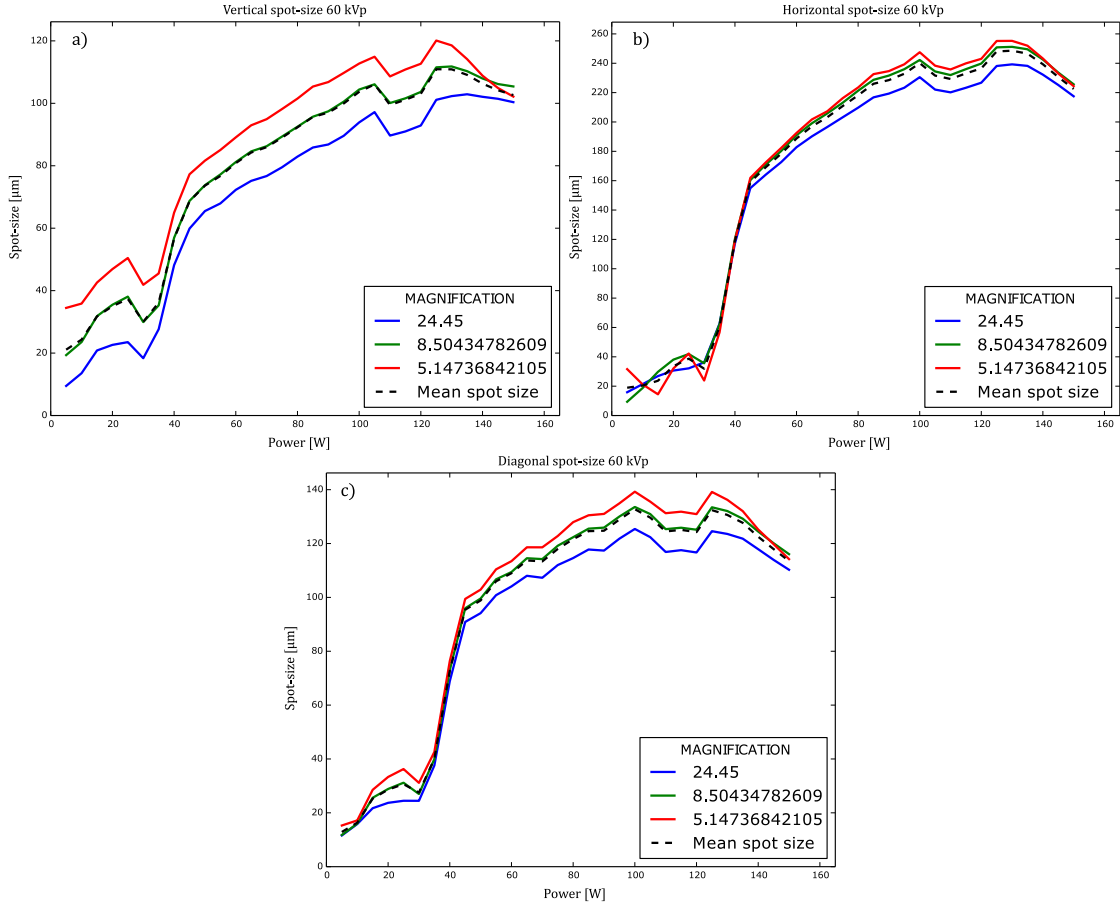


**Figure 5.4:** Illustration of The projected edge-profile with the associated fitted error-function, and the resulting Gauss-fits. Top: Plot of three projected edges and their corresponding error-function fit for three different magnifications, respectively. Bottom: Plot of the Gaussian functions fitted with the acquired fit parameter of the error-functions above. The FWHM of these fits is needed to determine the spot-size of the source.

the detector is needed. The extraction of the PSF out of the raw images is the same as for the other measurements and is for that reason not explained in further detail. Only for the detector PSF in the diagonal direction and their corresponding FWHM an additional step is needed. As the adjustment of the edge diagonal to the pixel was not possible, the PSF for this direction is determined using simple mathematical and geometrical considerations. The diagonal detector PSF is determined by quadratic multiplication of the vertical and horizontal detector PSF. With this at hand the spot-size of the source can be determined for the three directions. Therefore the equation 2.50 of section 2.3.3 is rearranged to:

$$\sigma_{source} = \frac{\sqrt{\sigma_{system}^2 - \sigma_{detector}^2}}{M - 1}, \quad (5.1)$$



and afterwards multiplied by  $2\sqrt{2\ln 2}$ , which finally yields to the FWHM of the source size in one direction and for one distinct power:

$$FWHM_{source} = \frac{\sqrt{FWHM_{system}^2 - FWHM_{detector}^2}}{M - 1}, \quad (5.2)$$

whereby  $M$  denotes the different magnification factors for the different distances of the source. With this equation the determination of the spot-size in the three different directions is possible. In the next section the results for the different measurements are discussed in further detail.

### 5.1.3 Results

#### Detector PSF

#### Source spot-size

#### Shape of the source-spot

## **5.2 Measurements using a Resolution-target**

### **5.2.1 Data acquisition**

**Measurement procedure**

### **5.2.2 Data processing**

## **6 Spectra measurements**



## 7 Comparison of different grating interferometer constellations

Setup	Period [ $\mu\text{m}$ ]	Height [ $\mu\text{m}$ ]	Material	$l$ [cm]	$d$ [cm]
Symmetric standard	$G_0$				
	$G_1$				
	$G_2$				
Symmetric standard	$G_0$				
	$G_1$				
	$G_2$				
Symmetric standard	$G_0$				
	$G_1$				
	$G_2$				
Symmetric standard	$G_0$				
	$G_1$				
	$G_2$				
Symmetric standard	$G_0$				
	$G_1$				
	$G_2$				
Symmetric standard	$G_0$				
	$G_1$				
	$G_2$				
Symmetric standard	$G_0$				
	$G_1$				
	$G_2$				

**Table 7.1:** Composition of the different setup configurations and their respective properties. The parameter for the inter grating distances  $l$  and  $d$  are adopted from Figure 2.3 to get a better imagination of the different setup dimensions. The distance between source and detector is fixed to 195.6 cm for all constellations, the duty cycle of all gratings is 0.5 and the phase shift of the used phase gratings is  $\pi/2$ . The results of the different performance fields of the particular setups are collocated in Table ??.



## **8 summary and outlook**

# List of Figures

2.1	Attenuation and phase shift of electromagnetic waves . . . . .	4
2.2	Simulated Talbot-carpets for a grating with a duty cycle of 0.5 a phase shift of $\pi/2$ and a grating period of $5 \mu m$ . . . . .	7
2.3	Sketch of a Talbot-Lau interferometer . . . . .	9
2.4	Different types of deep micro-structured gratings feasible for X-ray interferometry . . . . .	10
2.5	Simulated visibility as function of Talbot-distance $d_T$ . . . . .	13
2.6	Resulting data output generated by the stepping procedure. . . . .	16
2.7	Geometric magnification in curved wave setups . . . . .	17
2.8	Drawing of the edge in the centre of the beam for the measurement of the source size . . . . .	18
3.1	Rendering of the whole setup . . . . .	25
3.2	Dimensions of the source with focussing system . . . . .	27
3.3	Drawing of the relative distances between the particular parts of the setup	28
4.1	Dependency of the detector response onto the exposure time . . . . .	32
4.2	Time-stability of the source during two days . . . . .	33
4.3	Power-stability of the source with fixed energy to 60 kV . . . . .	34
5.1	Pictures of the knife edge and corresponding projection image . . . . .	38
5.2	Illustration of the different edge positions for the measurement . . . . .	39
5.3	Illustration of the projection of an edge profile . . . . .	41
5.4	Fit of the projection of the projected edge and corresponding Gauss-fits .	42

# List of Tables

2.1 Results for the mismatch due to a finite edge thickness $\Delta d$ at different magnifications . . . . .	20
7.1 Set of the properties of the different characterized setups . . . . .	47



# Acronyms

**AMP** Signal of the Amplitude modulation. 14, 15

**ASTM** ASTM International (former: American Society for Testing and Materials). 37

**CsI** Caesium Iodine. 29

**DCI** Dark-field Imaging. 15

**DPC** Differential Phase Contrast. 15

**EN** Europäische Norm. 37

**ESF** Edge spread function. 22, 23

**FWHM** full width at half maximum. 11, 23

**IEC** International Electrotechnical Commission. 37

**LIGA** Lithography and Galvanization. 9

**LSF** Line-spread-function. 22, 23

**LSI** linear and shift invariant. 21

**MTF** Modulation transfer function. 21, 22

**OTF** Optical transfer function. 21, 22

**PSF** Point-spread-function. 21–23

**PTF** Phase transfer function. 21



# Bibliography

- [1] ALS-NIELSEN, Jens: *Elements of Modern X-ray Physics*. Second Edi. A John Wiley & Sons, 2011. – ISBN 9780470973950
- [2] AMPTEC INC.: *Datasheet XR-100T-CdTe*
- [3] BAVENDIEK, Klaus ; EWERT, Uwe ; RIEDO, Adrian ; HEIKE, Uwe ; ZSCHERPEL, Uwe: New Measurement Methods of Focal Spot Size and Shape of X-ray Tubes in Digital Radiological Applications in Comparison to Current Standards. In: *18th World Conference on Nondestructive Testing* (2012), Nr. April, S. 16–20. – URL [http://212.8.206.21/article/wcndt2012/papers/346\\_wcndtfinal00346.pdf](http://212.8.206.21/article/wcndt2012/papers/346_wcndtfinal00346.pdf)
- [4] BECH, Martin: *PhD Thesis X-ray imaging with a grating interferometer*, University of Copenhagen Denmark, Dissertation, 2009. – 173 S
- [5] CREATH, Katherine: V Phase-Measurement Interferometry Techniques. In: *Progress in Optics* 26 (1988), Nr. C, S. 349–393. – ISBN 0079-6638
- [6] CREMER, Jay Theodore J.: *Neutron and X-ray Optics, Jay Theodore Cremer, Jr.*, Elsevier, 2013.pdf. First Edit. 2013. – 1124 S. – ISBN 9780124071599
- [7] CUNNINGHAM, I. a. ; FENSTER, a: *A method for modulation transfer function determination from edge profiles with correction for finite-element differentiation.*
- [8] DAVID, C. ; NÖHAMMER, B. ; SOLAK, H. H. ; ZIEGLER, E.: Differential x-ray phase contrast imaging using a shearing interferometer. In: *Applied Physics Letters* 81 (2002), Nr. 17, S. 3287. – URL <http://scitation.aip.org/content/aip/journal/apl/81/17/10.1063/1.1516611>. – ISSN 00036951
- [9] DONATH, Tilman: Quantitative X-ray Microtomography with Synchrotron Radiation. (2007), S. 209
- [10] KÖHLER, Jörg: Der Talbot-Effekt / Universität Regensburg, Institut für Experimentelle und Angewandte Physik. 2008. – Forschungsbericht. – 1–12 S
- [11] LEI, Yaohu ; DU, Yang ; LI, Ji ; ZHAO, Zhigang ; LIU, Xin ; GUO, Jinchuan ; NIU, Hanben: Fabrication of x-ray absorption gratings via micro-casting for grating-based phase contrast imaging. In: *Journal of Micromechanics and Microengineering* 24 (2014), Nr. 1, S. 015007. – URL <http://stacks.iop.org/0960-1317/24/i=1/a=015007?key=crossref.c8d5bae0afdef4852a68c7fb41ef568e>. – ISSN 0960-1317

- [12] LEWIS, Andrew J.: *Absolute length measurement using interferometry*, UNIVERSITY OF LONDON, IMPERIAL COLLEGE OF SCIENCE, TECHNOLOGY AND MEDICINE, 2002. – 324 S
- [13] LI, Ke ; ZAMBELLI, Joseph ; BEVINS, Nicholas ; GE, Yongshuai ; CHEN, Guang-Hong: Spatial resolution characterization of differential phase contrast CT systems via modulation transfer function (MTF) measurements. In: *Physics in medicine and biology* 58 (2013), Nr. 12, S. 4119–35. – URL <http://www.ncbi.nlm.nih.gov/pmc/articles/PMC3746757/> &tool=pmcentrez&rendertype=abstract. – ISBN 1361-6560 (Electronic) 0031-9155 (Linking)
- [14] LI, Ke ; ZAMBELLI, Joseph ; BEVINS, Nicholas ; GE, Yongshuai ; CHEN, Guang-Hong: Spatial resolution characterization of differential phase contrast CT systems via modulation transfer function (MTF) measurements. In: *Physics in medicine and biology* 58 (2013), Nr. 12, S. 4119–35. – URL <http://www.ncbi.nlm.nih.gov/pmc/articles/PMC3746757/> &tool=pmcentrez&rendertype=abstract. – ISBN 1361-6560 (Electronic) 0031-9155 (Linking)
- [15] LIU, Huiqiang ; WU, Xiseng: Optimization of reconstructed quality of hard x-ray phase microtomography. 54 (2015), Nr. 18, S. 5610–5618
- [16] MOMOSE, Atsushi: Recent Advances in X-ray Phase Imaging. In: *Japanese Journal of Applied Physics* 44 (2005), Nr. 9A, S. 6355–6367. – ISBN 0021-4922
- [17] MUELLER, Mark: Experimental characterization of the first preclinical X-ray phase contrast CT scanner. (2013)
- [18] PFEIFFER, F ; BECH, M ; BUNK, O ; KRAFT, P ; EIKENBERRY, E F. ; BRÖNNIMANN, Ch ; GRÜNZWEIG, C ; DAVID, C: Hard-X-ray dark-field imaging using a grating interferometer. In: *Nature materials* 7 (2008), Nr. 2, S. 134–137. – ISBN 1476-1122
- [19] PFEIFFER, Franz ; WEITKAMP, Timm ; BUNK, Oliver ; DAVID, Christian: Phase retrieval and differential phase-contrast imaging with low-brilliance X-ray sources. In: *Nature Physics* 2 (2006), Nr. 4, S. 258–261. – ISBN 1745-2473
- [20] PFEIFFER, Franz ; WEITKAMP, Timm ; DAVID, Christian: X-ray phase contrast imaging using a grating interferometer. In: *Europhysics News* 37 (2006), Nr. 5, S. 13–15. – ISSN 0531-7479
- [21] SAMEI, E ; FLYNN, M J. ; REIMANN, D a.: A method for measuring the presampled MTF of digital radiographic systems using an edge test device. In: *Medical physics* 25 (1998), Nr. 1, S. 102–113. – ISBN 0094-2405 (Print) 0094-2405 (Linking)
- [22] SCIENTIFIC CROSSROADS ; AMPTEC INC.: X R F F P S o f t w a r e G u i d e V.3.30. (2008)

- [23] SYSTEMS, Varian medical: *PaxScan ® 2520DX Digital Image Receptor*
- [24] TALBOT, Henry F.: Facts relating to Optical Science. In: *Philosophical Magazine and Journal of science* (1836)
- [25] VAN DER VEEN, Friso ; PFEIFFER, Franz: Coherent x-ray scattering. In: *Journal of Physics: Condensed Matter* 16 (2004), Nr. 28, S. 5003–5030. – ISBN 0953-8984\n1361-648X
- [26] WAGNER, Robert F.: Toward a unified view of radiological imaging systems. In: *Medical Physics* 1 (1974), Nr. 1, S. 11. – ISSN 00942405
- [27] WAGNER, Robert F.: Toward a unified view of radiological imaging systems. Part II: Noisy images. In: *Medical Physics* 4 (1977), Nr. 4, S. 279. – ISBN doi:10.1118/1.594362
- [28] WEITKAMP, Timm ; DAVID, Christian ; PFEIFFER, Franz: Tomography with grating interferometers at low-brilliance sources. (2006)
- [29] WEITKAMP, Timm ; DIAZ, Ana ; DAVID, Christian ; PFEIFFER, Franz ; STAM-PONI, Marco ; CLOETENS, Peter ; ZIEGLER, Eric: X-ray phase imaging with a grating interferometer. In: *Optics express* 13 (2005), Nr. 16, S. 6296–6304. – ISBN 1094-4087
- [30] X-RAY WORKX GMBH: *CAD Drawings XWT-160-SE ( 1 : 5 )*
- [31] X-RAY WORKX GMBH: *DATASHEET*. 2013
- [32] X-RAY WORKX GMBH: *X-COM software manual*. 2013
- [33] X-RAY WORKX GMBH: *MICROFOCUS X-RAY TUBES PRODUCT LINE SE*. 2015
- [34] XIN, Liu ; JIN-CHUAN, Guo ; XIANG, Peng ; HAN-BEN, Niu: Visibility in differential phase-contrast imaging with partial coherence source. In: *Chinese Physics* 16 (2007), Nr. 6, S. 1632–1636. – ISBN 1009-1963

